



CLASSY VII Ly α Profiles: The Structure and Kinematics of Neutral Gas and Implications for LyC Escape in Reionization-era Analogs*

Weida Hu¹, Crystal L. Martin¹, Max Gronke², Simon Gazagnes³, Matthew Hayes⁴, John Chisholm³, Timothy Heckman⁵, Matilde Mingozzi⁶, Namrata Roy⁵, Peter Senchyna⁷, Xinfeng Xu⁵, Danielle A. Berg³, Bethan L. James⁸, Daniel P. Stark⁹, Karla Z. Arellano-Córdova³, Alaina Henry^{5,6}, Anne E. Jaskot¹⁰, Nimisha Kumari⁸, Kaelee S. Parker³, Claudia Scarlata¹¹, Aida Wofford¹², Ricardo O. Amorín^{13,14}, Naunet Leonhardes-Barboza¹⁵, Jarle Brinchmann¹⁶, Cody Carr¹¹, and Alessandra Aloisi⁶

¹Department of Physics, University of California, Santa Barbara, Santa Barbara, CA 93106, USA

²Max-Planck Institute for Astrophysics, Karl-Schwarzschild-Str. 1, D-85741 Garching, Germany

³Department of Astronomy, The University of Texas at Austin, 2515 Speedway, Stop C1400, Austin, TX 78712, USA

⁴Stockholm University, Department of Astronomy and Oskar Klein Centre for Cosmoparticle Physics, AlbaNova University Centre, SE-10691, Stockholm, Sweden

⁵Center for Astrophysical Sciences, Department of Physics & Astronomy, Johns Hopkins University, Baltimore, MD 21218, USA

⁶Space Telescope Science Institute, 3700 San Martin Drive, Baltimore, MD 21218, USA

⁷Carnegie Observatories, 813 Santa Barbara Street, Pasadena, CA 91101, USA

⁸AURA for ESA, Space Telescope Science Institute, 3700 San Martin Drive, Baltimore, MD 21218, USA

⁹Steward Observatory, The University of Arizona, 933 N Cherry Avenue, Tucson, AZ 85721, USA

¹⁰Department of Astronomy, Williams College, Williams town, MA 01267, USA

¹¹Minnesota Institute for Astrophysics, University of Minnesota, 116 Church Street SE, Minneapolis, MN 55455, USA

¹²Instituto de Astronomía, Universidad Nacional Autónoma de México, Unidad Académica en Ensenada, Km 103 Carr. Tijuana-Ensenada, Ensenada 22860, Mexico

¹³Instituto de Investigación Multidisciplinar en Ciencia y Tecnología, Universidad de La Serena, Raul Bitrán 1305, La Serena 2204000, Chile

¹⁴Departamento de Astronomía, Universidad de La Serena, Av. Juan Cisternas 1200 Norte, La Serena 1720236, Chile

¹⁵Wellesley College, 106 Central Street, Wellesley, MA 02481, USA

¹⁶Instituto de Astrofísica e Ciências do Espaço, Universidade do Porto, CAUP, Rua das Estrelas, PT4150-762 Porto, Portugal

Received 2023 April 17; revised 2023 July 11; accepted 2023 July 27; published 2023 October 5

Abstract

Ly α line profiles are a powerful probe of interstellar medium (ISM) structure, outflow speed, and Lyman-continuum escape fraction. In this paper, we present the Ly α line profiles of the Cosmic Origins Spectrograph (COS) Legacy Archive Spectroscopic SurveY, a sample rich in spectroscopic analogs of reionization-era galaxies. A large fraction of the spectra show a complex profile, consisting of a double-peaked Ly α emission profile in the bottom of a damped, Ly α absorption trough. Such profiles reveal an inhomogeneous ISM. We successfully fit the damped Ly α absorption and the Ly α emission profiles separately, but with complementary covering factors, a surprising result because this approach requires no Ly α exchange between high- $N_{\text{H I}}$ and low- $N_{\text{H I}}$ paths. The combined distribution of column densities is qualitatively similar to the bimodal distributions observed in numerical simulations. We find an inverse relation between Ly α peak separation and the [O III]/[O II] flux ratio, confirming that the covering fraction of Lyman-continuum-thin sightlines increases as the Ly α peak separation decreases. We combine measurements of Ly α peak separation and Ly α red peak asymmetry in a diagnostic diagram, which identifies six Lyman-continuum leakers in the COS Legacy Archive Spectroscopic SurveY (CLASSY) sample. We find a strong correlation between the Ly α trough velocity and the outflow velocity measured from interstellar absorption lines. We argue that greater vignetting of the blueshifted Ly α peak, relative to the redshifted peak, is the source of the well-known discrepancy between shell-model parameters and directly measured outflow properties. The CLASSY sample illustrates how scattering of Ly α photons outside the spectroscopic aperture reshapes Ly α profiles because the distances to these compact starbursts span a large range.

Unified Astronomy Thesaurus concepts: Dwarf galaxies (416); Hubble Space Telescope (761); Stellar feedback (1602); Interstellar medium (847)

Supporting material: figure set, machine-readable tables

1. Introduction

The Epoch of Reionization (EoR) marks a period in the history of the Universe when the emergence of galaxies ionized most of

* Based on observations made with the NASA/ESA Hubble Space Telescope, obtained from the Data Archive at the Space Telescope Science Institute, which is operated by the Association of Universities for Research in Astronomy, Inc., under NASA contract NAS 5-26555.

Original content from this work may be used under the terms of the [Creative Commons Attribution 4.0 licence](https://creativecommons.org/licenses/by/4.0/). Any further distribution of this work must maintain attribution to the author(s) and the title of the work, journal citation and DOI.

the neutral hydrogen in the intergalactic medium (IGM). Observations suggest that the first ionized pockets in the IGM grew around the largest overdensities of galaxies (e.g., Tilvi et al. 2020; Hu et al. 2021; Hayes & Scarlata 2023). The massive stars in those galaxies are likely the source of the ionizing photons, the Lyman continuum (LyC) at wavelengths $\lambda < 912 \text{ \AA}$ (e.g., Robertson et al. 2015). How this ionizing radiation leaks out of the dense structures where early galaxies form, however, is not well understood. A small column density of neutral hydrogen, $N_{\text{H I}} \approx 1.6 \times 10^{17} \text{ cm}^{-2}$, will absorb a LyC photon. Exactly how feedback from massive stars opens pathways for LyC escape (Ma et al. 2020; Kakiichi & Gronke 2021) sets the timeline for

cosmic reionization (e.g., Finkelstein et al. 2019; Mason et al. 2019; Naidu et al. 2020). Direct observations of the escaping LyC photons are not possible during the EoR because of attenuation by the IGM (Ouchi et al. 2020, and references therein), so indirect tracers of LyC escape, and outflows are needed.

Ly α is the most commonly detected emission line from high-redshift galaxies (Partridge & Peebles 1967). The channels through which Ly α photons emerge from galaxies appear to be tightly related to the pathways of LyC escape (Chisholm et al. 2018; Gazagnes et al. 2020) because the origins of Ly α photons, H II regions, are illuminated by the LyC photons arising from central massive stars. Even low-column densities of neutral hydrogen in these channels scatter Ly α photons many times, altering their direction and frequency. Their random walk redistributes photons flux from the line core into the line wings, and this reshaping of the line profile imprints information about the outflow velocity, column density, and interstellar medium (ISM) structure on the emergent line profile (Verhamme et al. 2006, 2015; Dijkstra 2014; Chisholm et al. 2018; Gazagnes et al. 2020; Saldana-Lopez et al. 2022).

In the absence of absorption by dust, all the Ly α photons eventually escape from the galaxy, and radiative transfer calculations demonstrate some general properties of the line profiles. For example, analytic solutions for static slabs and spheres yield emerging Ly α spectra with symmetric redshifted and blueshifted peaks (Neufeld 1990; Dijkstra et al. 2006, 2016). Bulk motion requires Monte Carlo techniques, and these calculations demonstrate that outflowing gas produces an asymmetric profile, which has a stronger redshifted component regardless of the outflow geometry and structure (Verhamme et al. 2006, 2012).

The most commonly applied radiative transfer model, the homogeneous shell model, assumes an expanding, spherical shell of neutral hydrogen (Verhamme et al. 2006). Over a wide range of outflow properties, the emergent line profile has a P Cygni shape characterized by a redshifted emission line with a broad red wing plus a blueshifted absorption trough. For a very low H I column density, some emission from the near side of the thin shell is transmitted, producing blueshifted emission instead of absorption. Whereas a very-high-column density shell will trap a Ly α photon until it is eventually absorbed by a dust grain, and the emergent line profile has become that of a damped Ly α absorber (DLA), a completely dark absorption trough with very broad wings. The shell model does a good job of reproducing the diversity of commonly observed Ly α profile shapes (e.g., Verhamme et al. 2015; Gronke et al. 2017; Yang et al. 2017; Gurung-López et al. 2022). Statistically successful fits, however, do not guarantee an accurate recovery of outflow properties. The structure of the shell model is much simpler than actual ISM and multiphase outflows (Schneider & Robertson 2018; Gronke & Oh 2020; Fielding & Bryan 2022).

Low-ionization state (LIS) absorption lines in galaxy spectra unambiguously detect outflowing gas and have provided insight into how outflow properties vary with galaxy properties (Heckman et al. 2000, 2011; Martin et al. 2012, 2015; Chisholm et al. 2015). The outflow speeds derived from the blueshifts of these absorption lines offer an opportunity to test the shell model velocities, and the results reveal significant discrepancies both at high-redshift (Kulas et al. 2012) and among nearby Green Pea galaxies (Yang et al. 2017; Orlitová et al. 2018). Three major discrepancies are reported in those studies: (1) the best-fit redshifts are larger by 10–250 km s⁻¹ than the spectroscopic

redshifts; (2) the best-fit outflow velocities of expanding shell are lower than the outflow velocities derived by LIS lines; (3) the intrinsic Ly α line widths of shell model are broader than those of Balmer lines. Li & Gronke (2022) proposed that those discrepancies might be caused by the degeneracies between model parameters, but no explanation for these puzzles based on observations has been found.

We also draw attention to another limitation of the shell model. A large fraction of Green Peas and higher-redshift star-forming galaxies show Ly α emission line in the bottom of a DLA system (Reddy et al. 2016; McKinney et al. 2019). These profiles cannot be produced by a homogeneous shell model. The low-column density shells that produce double-peaked profiles contradict the presence of damped absorption, which requires very-high-column density. Even larger peak separations are predicted by a clumpy shell because the fitted shell expansion speed lies between the outflow velocities of the neutral clouds and the hot interclump medium (Li & Gronke 2022).

Comparing the physical properties derived from Ly α shell modeling to those measured from other spectral lines can therefore provide new insight about the structure of the multiphase gas. Because these properties determine the LyC escape fraction from galaxies, there is an urgent need to understand the puzzling properties of Ly α profiles in a sample of EoR analogs. To place the unexpected profile shapes, i.e., the double-peaked emission lines in DLA systems, in the broader context of the full diversity of observed Ly α profile shapes, requires high-resolution and high signal-to-noise ratio (S/N) UV spectroscopy of EoR analogs, including, but not limited to, Green Pea galaxies. The James Webb Space Telescope (JWST) observations reveal a diversity of galaxies in the EoR (e.g., Labbe et al. 2023; Bunker et al. 2023; Looser et al. 2023; Saxena et al. 2023; Tang et al. 2023), spanning much wider ranges of galaxy properties than those of the local Green Peas.

In this paper, we analyze 45 Ly α line profiles obtained by the Cosmic Origins Spectrograph (COS) Legacy Archive Spectroscopy Survey (CLASSY; Berg et al. 2022; James et al. 2022). This UV-surface brightness selected sample includes the lowest-redshift Green Pea galaxies, local Lyman break galaxy analogs (LBAs; Heckman et al. 2011), and the two local galaxies that are the nearest spectral match to the emission-line spectra of GN-z11 (Senchyna et al. 2023). Thus, the range in metallicity and ionizing continuum properties include the extreme conditions that were common during galaxy assembly. We present a uniform analysis of the Ly α profiles. The outflow properties have been determined from the blueshifted components of the LIS resonance lines (Xu et al. 2022) and the excited fine-structure lines (Xu et al. 2023). The results provide new insight into the clumpiness of the ISM, as described by the relative covering fractions of high- $N_{\text{H I}}$ and low- $N_{\text{H I}}$ gas, yet also strongly suggest that the discrepancies between shell-model parameters and LIS absorption lines arise from aperture vignetting. Among CLASSY targets, the physical size of COS aperture ranges from the scale of star clusters (~ 100 pc) to galaxies (~ 10 kpc). The large variations in aperture losses make it possible to view individual Ly α profile shapes in a broader context.

This paper is organized as follows. In Section 2, we introduce the CLASSY sample of Ly α profiles, describe how we remove the damped Ly α absorption and measure the properties of the high-column density neutral gas, and discuss the large variation in the amount of aperture vignetting across

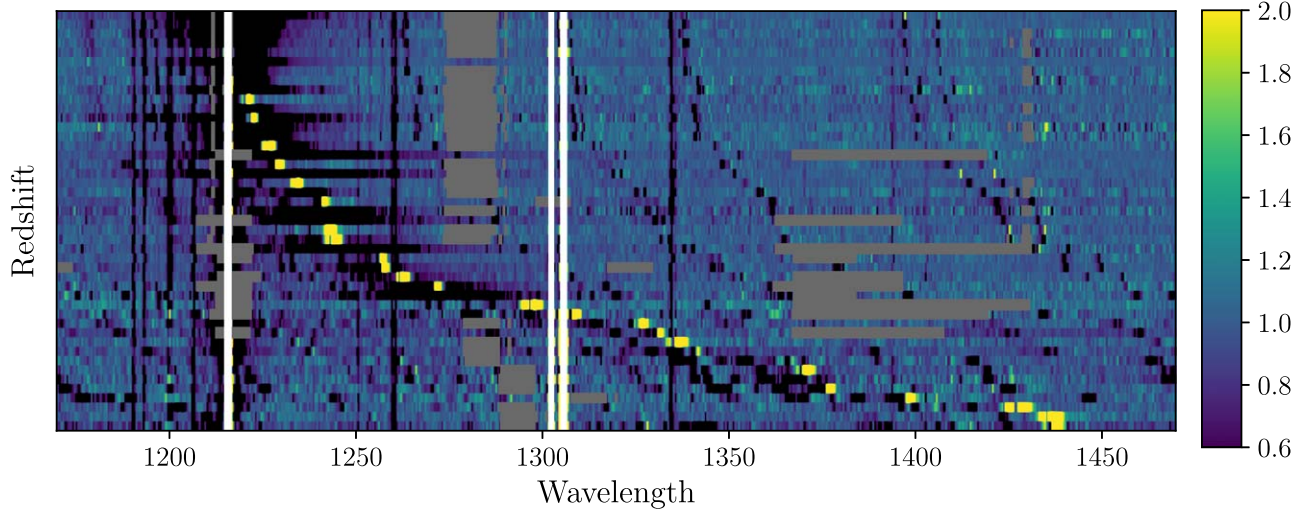


Figure 1. Overview of the COS G130M spectra obtained in the CLASSY survey with the wavelength coverage of 1170–1470 Å on the x-axis. The image is built by one continuum-normalized spectrum per image line. The redshift increases from top to bottom along the y-axis. The dark is low flux, and the yellow is high flux. The yellow waterfall highlights the redshifted Ly α emission lines. We use vertical white lines to mask the geocoronal Ly α and O II emission lines. The vertical dark lines indicate the MW absorption lines, and the gray strips indicate the CCD gaps.

the sample. In Section 3, we use the radiative transfer code `tlac` to fit shell models to the net Ly α emission-line profiles, investigating different choices for the continuum level (and hence the line equivalent width). In Section 4, we discuss the H I column density distribution in EoR analogs, the size scale of the holes leaking LyC radiation, and argue that the aperture vignetting biases the shell model properties in the directions required to solve the discrepancies with independently measured outflow properties.

Throughout this paper, we adopt a Flat Λ CDM cosmology with $\Omega_m = 0.3$, $\Omega_\Lambda = 0.7$, and $H_0 = 70 \text{ km s}^{-1} \text{ Mpc}^{-1}$. We also adopt the Spearman rank method to quantify the correlation strengths r . The data used in this paper are available via the CLASSY high-level science products (HLSP) homepage,¹⁷ including the best-fit DLA systems, the Ly α emission lines after subtracting the DLA and continuum, and the best-fit shell model spectra.

2. Sample of Ly α Profiles

Here, we present high-S/N Ly α spectra for the 45 CLASSY targets. Each of these nearby galaxies has a compact, far-UV bright star-forming region, which was the target of the COS observation. The sample provides a diverse set of local analogs of high-redshift galaxies, including both Green Pea galaxies and LBAs. The physical conditions in the starburst range cover oxygen abundances from $12 + \log(\text{O}/\text{H}) \sim 7$ to 8.8 and electron densities from $n_e \sim 10$ to 1120 cm^{-3} . The stellar masses and star formation rates of their host galaxies sample the range $\log(M_*/M_\odot) \sim 6.2$ to 10.1 and $\log(\text{SFR}/M_\odot \text{ yr}^{-1}) \sim -2$ –1.6, respectively (Berg et al. 2022). The raw spectroscopic data were reduced using the CALCOS pipeline (v3.3.10), including spectrum extraction, wavelength calibration, and vignetting correction, and then coadded using a custom pipeline (James et al. 2022). The Galactic foreground extinction was corrected assuming a ratio of total-to-selective extinction $R_V = 3.1$ and a Milky Way (MW) extinction curve (Cardelli et al. 1989).

Figure 1 shows an overview of the G130M and G160M spectra, ordered by redshift. The CLASSY spectra easily resolve the damping wings of the broad absorption trough imprinted by H I absorption from the MW. A large fraction of the spectra show a second DLA at the redshift of the CLASSY galaxy. In the lowest-redshift galaxies, the blueshifted damping wing of the target is blended with the redshifted damping wing of the MW absorption. The yellow waterfall across Figure 1 highlights the redshifted Ly α emission. Surprisingly, the Ly α emission is frequently detected in the bottom of a damped absorption trough. Profiles of this type cannot be produced by a uniform shell of neutral hydrogen.

In this paper, we adopt an approach that we have not seen used previously. We fit the damping wing profile, including a nonunity covering factor. We then extract the net emission-line profile relative to the damping trough, as others have done. The equivalent width of this net Ly α emission, however, has been previously neglected. We address this in Section 3.2 below, where we demonstrate that the best normalization for the Ly α emission is the fraction of the stellar continuum *not intercepted* by the high-column density neutral hydrogen.

We use physical models to define the continuum level near Ly α , allowing us to accurately model the DLA system in Section 2.1. CLASSY provides two models for the continuum (P. Senchyna et al. 2023, in preparation). Both models assume the observed continuum can be reconstructed as a linear combination of a set of single-age, single-metallicity stellar populations (Chisholm et al. 2019), and, thus, be fitted using the following relation:

$$F_{\text{obs}}(\lambda) = 10^{-0.4E(B-V)k(\lambda)} \sum_i X_i M_i(\lambda), \quad (1)$$

where $F_{\text{obs}}(\lambda)$ is the observed spectrum, $k(\lambda)$ is the attenuation law, $M_i(\lambda)$ is the spectrum of the i th single stellar population, and X_i is its coefficient. The main difference between the two methods is the stellar population synthesis framework. The top panels of Figure 2 illustrate each best-fit continuum. The red dashed line represents the continuum built from STARBURST 99 synthesis models (Leitherer et al. 1999) and

¹⁷ The data is available at the CLASSY HLSP page at DOI:10.17909/m3fq-jj25 and <https://archive.stsci.edu/hlsp/classy>.

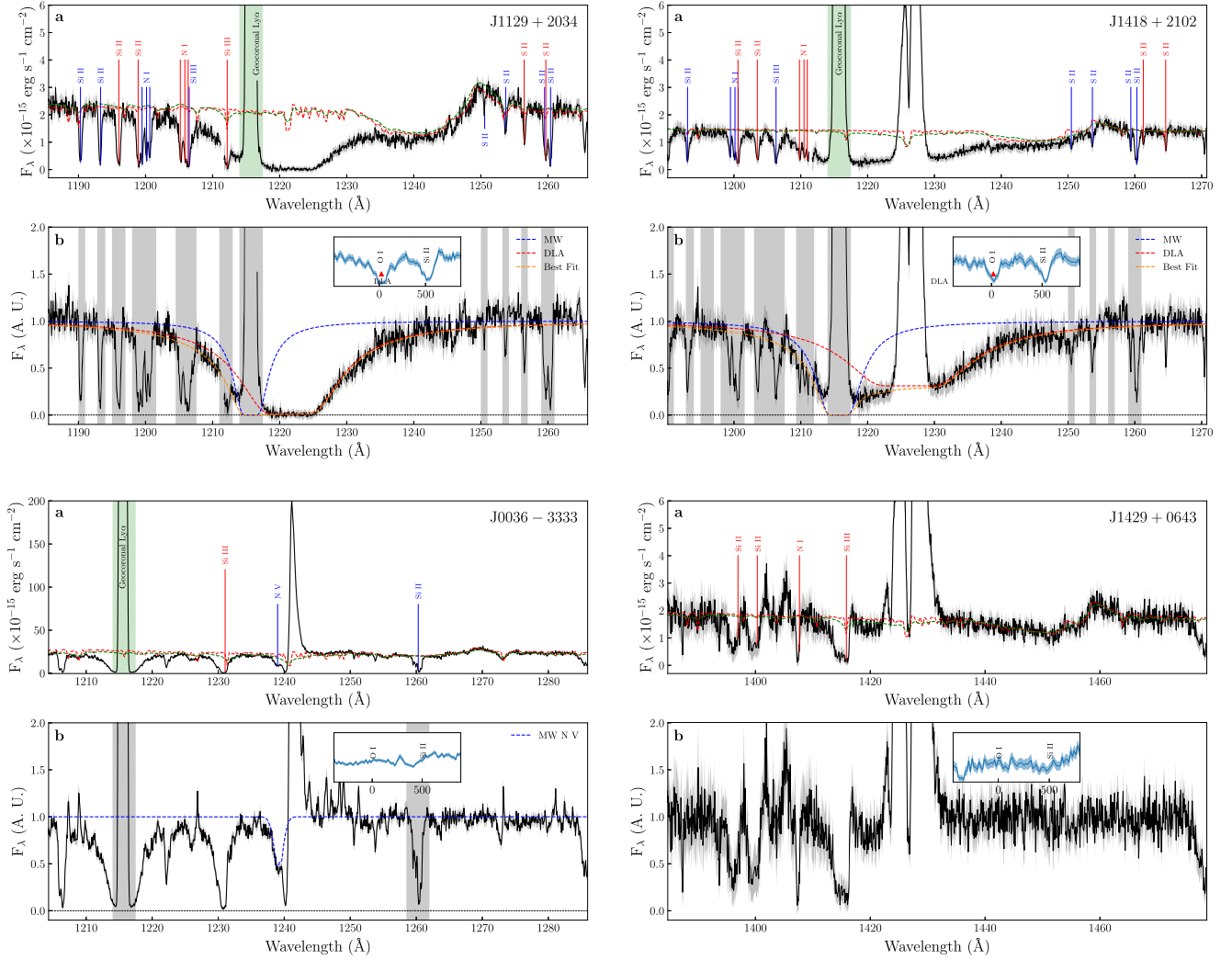


Figure 2. Examples of four typical Ly α profiles: pure DLA system, Ly α emission over DLA system, P Cygni-like Ly α emission, and pure Ly α emission. Panel (a): the flux spectra (black) and error spectra (gray shade) close to Ly α line. The vertical green shade masks the geocoronal Ly α emission line. The absorption lines are labeled in blue and red for absorption lines of MW and host galaxy, respectively. We overplot the best-fit continua in red and green dashed lines for the first and second methods (see Section 2). Panel (b): the best-fit absorption profiles (orange). The flux spectrum and error spectrum are normalized by the best-fit continuum (first method, red dashed line in panel (a)). We mask the absorption lines (vertical gray shades) and Ly α emission line and use two components to fit the absorption profile, which corresponds to the MW component (blue) and a host-galaxy DLA component (red). For the host-galaxy component, we adopt a Voigt profile. For the MW component, we adopt a Voigt profile if it is an MW DLA system with fixed galactic H I column density (Hartmann & Burton 1997), or a Gaussian profile if it is an MW metal absorption line. The small inset shows the O I λ 1302 Å absorption line. (The complete figure set of 45 images is available.)

a Reddy et al. (2016) attenuation law, and the green dashed line uses the latest version of the Bruzual & Charlot (2003) model (S. Charlot & G. Bruzual 2023, in preparation; see also Plat et al. 2019) and an SMC extinction law (Gordon et al. 2003). These two continua both reproduce the prominent N V λ 1240 stellar P Cygni line well. The narrow dip visible at Ly α in both models is not physical (C. Leitherer 2023, private communication), and we interpolate over it. We fit the DLA profiles using both the continuum models and found similar parameters. We adopt the first method for the analysis that follows because the STARBURST99 models have the higher spectral resolution.

2.1. DLA Fitting

Figure 2 illustrates the diversity of CLASSY Ly α profiles: pure DLA systems, Ly α emission in the bottom of a damping

trough (hereafter Abs+EM profile), P Cygni-like profiles, and double-peaked Ly α emission. A large fraction of CLASSY spectra (31/45) have a DLA system, and 20 out of these 31 galaxies show double- or single-peaked Ly α emission lines. CLASSY spectra offer the high spectral resolution and S/N required to remove the contribution of the DLA system (e.g., Reddy et al. 2016; McKinney et al. 2019) and extract the Ly α emission lines.

Figure 1 shows that geocoronal emission lines intersect the broad damping wings at low-redshift and at $z \approx 0.07$. In addition, the LIS absorption lines from the MW and the target galaxy affect the wings of the DLA systems but intersect only a few Ly α emission lines (see Section 2.1.2). We mask these lines as indicated in the second row of Figure 2.

To uniquely describe the MW DLA system, we adopt the Galactic H I column density derived from 21 cm emission in the direction of the target (Hartmann & Burton 1997). The

DLA line profile is described by a Voigt profile (e.g., Prochaska 2019), which is defined by a Doppler parameter (b) and a column density (N_{HI}). We assume a Doppler parameter of 30 km s^{-1} (e.g., Prochaska et al. 2015), no velocity shift, and complete covering of the continuum source. These steps define the Voigt profile, which we convolve with the instrumental resolution, and then subtract from the normalized continuum to uncover the Ly α profile of the CLASSY target.

Because DLA systems are optically thick, the bottom of the Voigt profile is completely dark. However, we found significant residual intensity in the bottom of the damping troughs. A partial covering of the continuum source therefore turns out to be critical for fitting damping profiles. This partial covering was sometimes subtle, as in the top left panel (J1129+2034) of Figure 2. In contrast, the top right panel (J1418+2102) of Figure 2 shows strong HI damping wings and prominent residual intensity in the trough. Here, we adopt a modified Voigt profile, which allows a velocity offset, v , and a velocity-independent covering fraction, f_c .

We convolve each Voigt profile with a Gaussian line spread function whose width is determined by the spectral resolution (Table 3 in Berg et al. 2022). Our fitting code then multiplies the normalized continuum by the optical depth of each Voigt profile. The error is measured using a Monte Carlo (MC) approach; we add random noise to the observed spectra and refit it 1000 times. Leaving all the parameters free provided statistically good fits; however, we noticed degeneracies between the fitted velocity v of the DLA and the wings of the damping profile, and also the overlaps between the wings of the DLA system and Ly α emission.

We broke these degeneracies by using the O I $\lambda 1302.2 \text{ \AA}$ absorption line to constrain the parameters of the Voigt profile, an approach Section 2.1.1 justifies below. The profile shape is not sensitive to b , and we fixed b to be 30 km s^{-1} . The second row of Figure 2 presents the continuum-normalized spectra, our model for the MW absorption, and the fitted damped Ly α absorption. Table 1 summarizes the best-fit Voigt parameters for the DLAs.

We extract the Ly α emission lines by subtracting the stellar continuum and DLA profile. Previous works have visually selected a local continuum close to the Ly α emission. A comparison of common targets shows that the resulting Ly α can be sensitive to the wavelength range used to define the local continuum. For example, the beginning of the wavelength range of J0938+5428 used in Alexandroff et al. (2015) is the Ly α blue peak of J0938+5428 in Figure 2. For this same target, Yang et al. (2017) determine the wavelength range from the intersection of the Ly α emission line with the DLA profile. This method recovers the Ly α blue peak; however, it underestimates the Ly α flux because the bottom of the DLA system is poorly estimated.

Among 45 CLASSY galaxies, 24 galaxies show significant double-peak Ly α emission lines, and 10 show single-peak Ly α emission. Figure 3 presents the Ly α emission-line spectra of 34 CLASSY galaxies. The remaining 11 galaxies show pure DLA systems, and are therefore not included in Figure 3.

2.1.1. Constraining the DLA Properties with O I Absorption

We use the narrow O I absorption lines to constrain the velocity of the DLA. Since the ionization potentials of O and H are very similar, we expect the O I to trace H I gas in the DLA

absorber. Figure 4 validates this expectation; the DLA systems in CLASSY always associate with strong O I absorption. The only O I absorber without a DLA is J1112+5503, which shows a P Cygni Ly α profile still suggesting substantial H I gas.

For optically thick O I absorption, the residual flux at the bottom of the fitted Gaussian profile determines the covering fraction of O I gas. The O I optical depth can be measured following

$$\tau = 0.318 \left(\frac{N_{\text{OI}}}{10^{14} \text{ cm}^{-2}} \right) \left(\frac{30 \text{ km s}^{-1}}{b} \right), \quad (2)$$

where N_{OI} is the O I column density, and b is the Doppler parameter (Draine 2011). Since the H I column densities of DLAs in the CLASSY sample are $>10^{20} \text{ cm}^{-2}$, and the metallicities $12+\log(\text{O}/\text{H})$ are >7.5 , we find that the O I optical depths are >10 , and the line is saturated. We acknowledge that this argument relies on the assumption that O I is uniformly distributed in the neutral gas. If the intervening O I clouds have different velocities, the covering fraction derived from O I absorption would place a lower limit on the covering fraction of neutral gas (Rivera-Thorsen et al. 2015).

Figure 5 shows that the O I covering fraction is approximately equal to the covering fraction of the DLA system. Table 1 collects the best-fit velocities and covering fractions for the DLA and O I absorption.

2.1.2. Notes on Individual Galaxies

1. The bottom of the DLA system is hidden under the Ly α emissions in J0938+5428, J1024+0524, J1416+1223, and J1521+0759 in their plots; see the online component of Figure 2, so the residual flux in the damping trough is not directly constrained. Since the blue wing of the damping profile is contaminated by metal absorption lines, the shape of the damping profile is poorly constrained. Therefore, for these four galaxies, we adopt the O I covering fractions to be their DLA covering fractions.
2. The covering fractions of four galaxies (J0337-0502, J0405-3648, J1132+1411, J1448-0110) are fixed to be a constant measured visually but also in agreement with their O I covering fractions. The Voigt profile fit for these four galaxies underestimates the covering fraction because the CLASSY error spectra do not account for the small counts at the trough bottom, which produce an asymmetric error (Cash 1979).
3. The DLA systems of three galaxies (J0127-0619, J1044+0353, J1359+5726) were not fitted well by a single Voigt profile, and we noticed that their O I absorption lines show a second component. Thus, we adopted two Voigt profiles and matched their velocities and covering factors to those of the O I components.
4. In J1105+4444, the Ly α peak separation is exceptionally broad, $\sim 1000 \text{ km s}^{-1}$. We suggest that the peaks are likely emitted by different regions within the COS aperture. To test this conjecture, we inspected Hubble Space Telescope (HST)/COS NUV acquisition image (see Figure 3 in Berg et al. 2022). We found that J1105+4444 is not only an elongated object with multiple clumps, but also the major axis of these clumps is along the dispersion direction of the COS observation. Thus, their spatial offset in the aperture may cause an apparent

Table 1
DLA Measurements

Object	z_{spec}	D_L^a (Mpc)	$f_{c,\text{DLA}}$	$f_{c,\text{O I}}$	$\log N_{\text{H}}$ (cm^{-2})	v (km s^{-1})	COS Aperture Size (kpc)
(1)	(2)	(3)	(4)	(5)	(6)	(7)	8
J0021+0052	0.09839	452	4.5
J0036-3333	0.02060	80	0.93
J0127-0619	0.00540	18	0.08 ± 0.04	0.38 ± 0.15	21.21 ± 0.27	-189 ± 14	0.22
			0.92 ± 0.04	0.93 ± 0.06	21.04 ± 0.03	11 ± 5	
J0144+0453	0.00520	17	0.96 ± 0.01	0.78 ± 0.05	20.18 ± 0.02	42 ± 7	0.2
J0337-0502	0.01352	51	1.00	0.76 ± 0.03	21.81 ± 0.00	-18 ± 3	0.61
J0405-3648	0.00280	11	>0.99	... ^d	20.80 ± 0.02	-35 ± 17^b	0.13
J0808+3948	0.09123	417	4.2
J0823+2806	0.04722	210	0.99 ± 0.01	0.98 ± 0.02	21.61 ± 0.03	22 ± 20	2.3
J0926+4427	0.18067	875	7.6
J0934+5514	0.00250	12	0.98 ± 0.00	0.38 ± 0.02^d	21.24 ± 0.00	23 ± 3	0.14
J0938+5428	0.10210	471	0.80 ± 0.05^c	0.80 ± 0.05	20.34 ± 0.08	3 ± 13	4.7
J0940+2935	0.00168	10	0.95 ± 0.01	0.69 ± 0.06^d	21.26 ± 0.01	-51 ± 7	0.12
J0942+3547	0.01486	65	0.76
J0944-0038	0.00478	24	0.84 ± 0.03	0.88 ± 0.15	21.67 ± 0.05	7 ± 24	0.29
J0944+3442	0.02005	86	0.92 ± 0.01	0.85 ± 0.11	21.51 ± 0.03	13 ± 23	1
J1016+3754	0.00388	20	0.24
J1024+0524	0.03319	143	0.54 ± 0.05^c	0.54 ± 0.05	20.58 ± 0.07	-72 ± 13	1.6
J1025+3622	0.12650	593	0.47 ± 0.12	0.56 ± 0.05	20.69 ± 0.19	-151 ± 34	5.7
J1044+0353	0.01287	60	0.09 ± 0.03	0.50 ± 0.09	20.08 ± 0.44	-101 ± 75	0.71
			0.91 ± 0.03	0.91 ± 0.05	21.84 ± 0.03	-29 ± 9	
J1105+4444 ^e	0.02154	92	0.42 ± 0.07	...	20.88 ± 0.09	-121 ± 31	1.1
			0.58 ± 0.07	...	21.87 ± 0.07	-54 ± 85	
J1112+5503	0.13164	619	5.9
J1119+5130	0.00446	22	0.80 ± 0.02	0.68 ± 0.04	20.77 ± 0.03	-2 ± 8	0.26
J1129+2034	0.00470	27	0.99 ± 0.01	0.87 ± 0.04	21.11 ± 0.01	23 ± 5	0.32
J1132+5722	0.00504	24	1.00 ± 0.01	0.71 ± 0.11	21.24 ± 0.02	17 ± 15	0.29
J1132+1411	0.01764	74	1.00	0.98 ± 0.01	20.53 ± 0.01	-40 ± 4	0.87
J1144+4012	0.12695	595	0.92 ± 0.03	0.91 ± 0.03	20.52 ± 0.06	-225 ± 36	5.7
J1148+2546	0.04512	195	0.78 ± 0.02	0.93 ± 0.06	21.19 ± 0.03	-75 ± 11	2.2
J1150+1501	0.00245	11	0.89 ± 0.00	0.81 ± 0.03^d	21.04 ± 0.01	10 ± 5	0.13
J1157+3220	0.01097	52	0.62
J1200+1343	0.06675	300	3.2
J1225+6109	0.00234	10	0.96 ± 0.01	... ^d	21.26 ± 0.01	11 ± 5^b	0.12
J1253-0312	0.02272	100	0.47 ± 0.01	0.62 ± 0.04	21.41 ± 0.04	-45 ± 6	1.2
J1314+3452	0.00288	12	0.95 ± 0.01	0.92 ± 0.02^d	20.71 ± 0.01	-39 ± 2	0.15
J1323-0132	0.02246	93	1.1
J1359+5726	0.03383	140	0.56 ± 0.4	0.50 ± 0.02	20.07 ± 0.11	-306 ± 17	1.6
			0.34 ± 0.1	0.82 ± 0.04	21.44 ± 0.15	-106 ± 10	
J1416+1223	0.12316	576	0.80 ± 0.05^c	0.80 ± 0.05	20.19 ± 0.05	16 ± 13	5.5
J1418+2102	0.00855	40	0.70 ± 0.02	0.79 ± 0.07	21.30 ± 0.03	18 ± 6	0.48
J1428+1653	0.18167	881	7.6
J1429+0643	0.17350	837	7.4
J1444+4237	0.00230	9	0.98 ± 0.00	0.44 ± 0.3^d	21.57 ± 0.01	-46 ± 8	0.11
J1448-0110	0.02741	111	>0.99	0.95 ± 0.03	21.56 ± 0.01	23 ± 5	1.3
J1521+0759	0.09426	432	0.49 ± 0.06^c	0.49 ± 0.06	20.42 ± 0.11	-85 ± 19	4.4
J1525+0757	0.07579	343	3.6
J1545+0858	0.03772	159	0.40 ± 0.02	0.63 ± 0.1	21.54 ± 0.04	-25 ± 12	1.8
J1612+0817	0.14914	709	6.5

Notes. (1) Object name; (2) spectroscopic redshift from Berg et al. (2022); (3) luminosity distance; (4) covering fraction of DLA absorber; (5) covering fraction of O I absorption; (6) column density of DLA absorber; (7) velocity of O I absorption line (except J1105+4444); (8) physical size of COS aperture.

^a The luminosity distances have been corrected for cosmic flow using `Cosmicflows-3` model <http://edd.ifa.hawaii.edu/> (Kourkchi et al. 2020). We adopt the CF3 model, as it considers several mass concentrations, including the Virgo Cluster, the Great Attractor, etc., and provides distance–velocity relation for every random galaxy at distance within 200 Mpc.

^b The velocity of O I absorber is measured using C II absorption line.

^c The covering fraction of DLA absorber is measured using O I absorption line.

^d The covering fraction of O I might be underestimated due to contamination of geocoronal O I emission line.

^e The Voigt parameters of J1105+4444 are fitted using two free velocities. For more details, see Section 2.1.2.

(This table is available in machine-readable form.)

Table 2
Ly α Measurements

Object	$f_{\text{Ly}\alpha}$ (10^{-15} erg s $^{-1}$ cm $^{-2}$)	$\log L_{\text{Ly}\alpha}$ (erg s $^{-1}$)	$\text{EW}_{\text{Ly}\alpha}$ (Å)	$f_{\text{esc}}^{\text{Ly}\alpha}$ (%)	A_f	$\Delta v_{\text{Ly}\alpha}$ (km s $^{-1}$)	$v_{\text{Ly}\alpha}^{\text{blue}}$ (km s $^{-1}$)	$v_{\text{Ly}\alpha}^{\text{red}}$ (km s $^{-1}$)	$v_{\text{Ly}\alpha}^{\text{trough}}$ (km s $^{-1}$)	$f_{\text{Ly}\alpha}^{\text{blue}}$ (10^{-15} erg s $^{-1}$ cm $^{-2}$)	$f_{\text{Ly}\alpha}^{\text{red}}$ (10^{-15} erg s $^{-1}$ cm $^{-2}$)
(1)	(2)	(3)	(4)	(5)	(6)	(7)	(8)	(9)	(10)	(11)	(12)
Double Peaks											
J0021+0052	144.56 \pm 1.43	42.5	29.04 \pm 0.29	25 \pm 0.45	2.91 \pm 0.04	571 \pm 54	-419 \pm 53	152 \pm 12	-27 \pm 20	8.4 \pm 0.5	136.4 \pm 1.4
J0808+3948	64.31 \pm 0.52	42.1	15.02 \pm 0.12	27 \pm 0.22	1.29 \pm 0.12	507 \pm 28	-470 \pm 26	37 \pm 9	-312 \pm 6	3.2 \pm 0.2	61.2 \pm 0.5
J0926+4427	64.64 \pm 0.56	42.8	40.65 \pm 0.35	35 \pm 0.67	1.42 \pm 0.13	427 \pm 52	-203 \pm 45	224 \pm 25	-47 \pm 17	7.5 \pm 0.2	57.1 \pm 0.5
J0938+5428	21.14 \pm 0.52	41.7	4.06 \pm 0.10	3.2 \pm 0.083	1.93 \pm 0.19	669 \pm 52	-296 \pm 41	373 \pm 31	116 \pm 32	7.4 \pm 0.3	13.8 \pm 0.4
J0942+3547	97.61 \pm 0.31	40.7	17.95 \pm 0.06	18 \pm 0.093	1.53 \pm 0.15	267 \pm 16	-113 \pm 14	154 \pm 7	-16 \pm 7	14.6 \pm 0.3	82.6 \pm 0.4
J0944-0038	20.47 \pm 0.43	39.2	9.95 \pm 0.21	4.1 \pm 0.085	0.86 \pm 0.35	416 \pm 65	-150 \pm 61	267 \pm 23	34 \pm 82	3.4 \pm 0.7	17.1 \pm 0.8
J0944+3442	0.43 \pm 0.09	38.6	0.56 \pm 0.11	0.82 \pm 0.17	1.71 \pm 0.59	531 \pm 99	-273 \pm 67	257 \pm 76	-20 \pm 150	0.1 \pm 0.1	0.4 \pm 0.1
J1016+3754	146.06 \pm 1.74	39.8	15.42 \pm 0.18	12 \pm 0.16	1.51 \pm 0.21	404 \pm 45	-230 \pm 43	175 \pm 13	-34 \pm 22	12.2 \pm 0.9	133.9 \pm 1.4
J1024+0524	54.13 \pm 0.50	41.1	8.72 \pm 0.08	5 \pm 0.097	2.87 \pm 0.08	464 \pm 36	-338 \pm 35	126 \pm 8	-64 \pm 18	2.1 \pm 0.3	52.1 \pm 0.5
J1025+3622	53.28 \pm 0.62	42.3	21.95 \pm 0.25	17 \pm 0.25	1.70 \pm 0.15	469 \pm 43	-263 \pm 39	206 \pm 17	-100 \pm 25	4.5 \pm 0.2	48.8 \pm 0.6
J1044+0353	1.55 \pm 0.08	38.8	0.90 \pm 0.05	0.096 \pm 0.005	1.84 \pm 0.36	425 \pm 119	-293 \pm 111	132 \pm 45	-123 \pm 98	0.2 \pm 0.1	1.3 \pm 0.1
J1105+4444	2.52 \pm 0.18	39.4	0.53 \pm 0.04	0.072 \pm 0.0051	...	999 \pm 109	-517 \pm 76	482 \pm 76	-204 \pm 244	0.4 \pm 0.2	2.2 \pm 0.2
J1119+5130	2.30 \pm 0.16	38.1	0.71 \pm 0.05	0.78 \pm 0.053	4.20 \pm 0.27	649 \pm 76	-337 \pm 67	312 \pm 34	-67 \pm 108	1.2 \pm 0.2	1.1 \pm 0.1
J1148+2546	12.34 \pm 0.23	40.7	5.62 \pm 0.10	7.4 \pm 0.14	1.92 \pm 0.46	717 \pm 97	-450 \pm 73	268 \pm 63	-132 \pm 58	0.4 \pm 0.1	12.0 \pm 0.2
J1200+1343	80.54 \pm 0.44	41.9	56.87 \pm 0.31	9.3 \pm 0.11	2.68 \pm 0.05	530 \pm 21	-394 \pm 20	136 \pm 5	-48 \pm 20	9.0 \pm 0.2	71.6 \pm 0.4
J1253-0312	338.94 \pm 1.21	41.6	32.14 \pm 0.12	4.4 \pm 0.032	1.48 \pm 0.11	433 \pm 14	-214 \pm 11	219 \pm 8	-46 \pm 9	37.7 \pm 0.5	301.1 \pm 1.1
J1323-0132	190.14 \pm 0.56	41.3	81.19 \pm 0.24	21 \pm 0.1	1.78 \pm 0.06	168 \pm 12	-95 \pm 12	74 \pm 1	-35 \pm 7	45.0 \pm 1.5	142.7 \pm 1.5
J1416+1223	11.70 \pm 0.47	41.7	3.26 \pm 0.13	3 \pm 0.13	1.75 \pm 0.28	613 \pm 91	-315 \pm 80	298 \pm 43	35 \pm 51	6.0 \pm 0.4	5.7 \pm 0.3
J1418+2102	26.76 \pm 0.22	39.7	19.14 \pm 0.16	2.4 \pm 0.021	1.10 \pm 0.18	403 \pm 26	-122 \pm 25	281 \pm 9	25 \pm 9	7.6 \pm 0.2	19.0 \pm 0.2
J1428+1653	38.94 \pm 0.82	42.6	12.32 \pm 0.26	27 \pm 1	3.34 \pm 0.34	416 \pm 84	-328 \pm 76	89 \pm 38	-109 \pm 66	2.6 \pm 0.3	36.4 \pm 0.8
J1429+0643	67.53 \pm 0.90	42.8	33.22 \pm 0.44	11 \pm 0.18	3.56 \pm 0.15	545 \pm 72	-292 \pm 67	253 \pm 25	54 \pm 33	15.2 \pm 0.5	52.4 \pm 0.7
J1448-0110	0.43 \pm 0.13	38.8	0.09 \pm 0.03	0.027 \pm 0.0083	...	395 \pm 153	-354 \pm 124	40 \pm 91	-283 \pm 134	0.1 \pm 0.1	0.3 \pm 0.1
J1521+0759	27.21 \pm 0.64	41.8	4.85 \pm 0.11	12 \pm 0.52	3.27 \pm 0.09	404 \pm 48	-247 \pm 45	157 \pm 16	-68 \pm 29	-1.0 \pm 0.4	28.4 \pm 0.7
J1545+0858	160.58 \pm 1.02	41.7	29.26 \pm 0.19	7.5 \pm 0.048	2.75 \pm 0.08	284 \pm 14	-122 \pm 10	163 \pm 10	-27 \pm 15	6.4 \pm 0.3	154.2 \pm 1.0
Single Peak / P Cygni											
J0036-3333	175.93 \pm 1.20	41.1	7.13 \pm 0.05	9.2 \pm 0.063	100 \pm 5	175.9 \pm 1.2
J0940+2935	0.58 \pm 0.06	36.8	0.34 \pm 0.03	0.46 \pm 0.044	273 \pm 57	0.6 \pm 0.1
J1112+5503	12.43 \pm 0.45	41.8	5.45 \pm 0.20	3.8 \pm 0.15	143 \pm 47	12.4 \pm 0.4
J1144+4012	2.50 \pm 0.21	41.0	1.75 \pm 0.15	1.6 \pm 0.14	318 \pm 70	2.5 \pm 0.2
J1157+3220	389.02 \pm 2.53	41.1	21.63 \pm 0.14	23 \pm 0.2	50 \pm 13	389.0 \pm 2.5
J1225+6109	0.50 \pm 0.21	36.8	0.04 \pm 0.02	0.016 \pm 0.0065	52 \pm 63	0.5 \pm 0.2
J1314+3452	0.85 \pm 0.06	37.2	0.21 \pm 0.01	0.027 \pm 0.0018	210 \pm 47	0.8 \pm 0.1
J1359+5726	72.71 \pm 0.68	41.2	8.71 \pm 0.08	6.7 \pm 0.081	148 \pm 16	72.7 \pm 0.7
J1525+0757	67.41 \pm 1.21	42.0	14.92 \pm 0.27	16 \pm 0.43	82 \pm 7	67.4 \pm 1.2
J1612+0817	36.97 \pm 0.83	42.3	12.71 \pm 0.29	7 \pm 0.18	114 \pm 14	37.0 \pm 0.8

Note. (1) Object name; (2) Ly α flux; (3) Ly α luminosity; (4) Ly α equivalent width; (5) Ly α escape fraction; (6) Ly α red peak asymmetry; (7) Ly α peak separation; (8) Ly α blue peak velocity offset; (9) Ly α red peak velocity offset; (10) Ly α trough velocity offset; (11) Ly α blue peak flux; (12) Ly α red peak flux. We note that the luminosity distances of some galaxies used in this work are different with those in Berg et al. (2022) because of the correction of cosmic flow. The properties (e.g., stellar mass, star formation rate) of those galaxies, which rely on the luminosities, are scaled accordingly.

(This table is available in machine-readable form.)

Table 3
Ancillary Data

Object	f_{1500} (10^{-15} erg s $^{-1}$ cm $^{-2}$)	M_{1500}	Z_{neb}	$\log M_*$ (M_{\odot})	$E(B - V)$	O32	$v_{\text{Si II}}^{\text{outflow}}$ (km s $^{-1}$)	r_{50} ($''$)
(1)	(2)	(3)	(4)	(5)	(6)	(7)	(8)	(9)
J0021+0052	3.94	-20.55	8.17 ± 0.07	9.09 $^{+0.18}_{-0.38}$	0.13 ± 0.006	2.0 ± 0.1	231 $^{+77}_{-77}$	0.25
J0036-3333	16.60	-18.34	8.21 ± 0.17	9.09 $^{+0.26}_{-0.23}$	0.30 ± 0.012	1.1 ± 0.1	157 $^{+22}_{-22}$	0.28
J0127-0619	4.04	-13.58	7.68 ± 0.02	8.63 $^{+0.18}_{-0.15}$	0.48 ± 0.006	1.1 ± 0.1	...	0.15
J0144+0453	1.87	-12.63	7.76 ± 0.02	7.52 $^{+0.24}_{-0.29}$	0.04 ± 0.030	2.1 ± 0.1	48 $^{+16}_{-16}$	3.54
J0337-0502	7.99	-16.60	7.46 ± 0.04	7.01 $^{+0.24}_{-0.21}$	0.05 ± 0.006	6.2 ± 0.2	...	1.62
J0405-3648	0.96	-10.90	7.04 ± 0.05	6.60 $^{+0.28}_{-0.28}$	0.11 ± 0.005	0.6 ± 0.1	...	6.43
J0808+3948	3.42	-20.23	8.77 ± 0.12	9.12 $^{+0.30}_{-0.17}$	0.24 ± 0.070	0.8 ± 0.1	646 $^{+65}_{-65}$	0.08
J0823+2806	3.85	-18.86	8.28 ± 0.01	9.38 $^{+0.33}_{-0.19}$	0.21 ± 0.004	2.0 ± 0.1	136 $^{+45}_{-45}$	0.28
J0926+4427	1.14	-20.64	8.08 ± 0.02	8.76 $^{+0.30}_{-0.26}$	0.10 ± 0.008	3.1 ± 0.1	353 $^{+52}_{-52}$	0.23
J0934+5514	15.10	-14.05	6.98 ± 0.01	6.25 $^{+0.15}_{-0.20}$	0.07 ± 0.007	8.7 ± 0.1	112 $^{+37}_{-37}$	1.53
J0938+5428	3.56	-20.53	8.25 ± 0.02	9.15 $^{+0.18}_{-0.29}$	0.13 ± 0.006	1.9 ± 0.1	215 $^{+72}_{-72}$	0.28
J0940+2935	1.45	-11.14	7.66 ± 0.07	6.80 $^{+0.23}_{-0.40}$	0.06 ± 0.010	0.7 ± 0.1	102 $^{+34}_{-34}$	3.06
J0942+3547	3.80	-16.30	8.13 ± 0.03	7.56 $^{+0.21}_{-0.29}$	0.06 ± 0.011	2.6 ± 0.1	97 $^{+26}_{-26}$	0.33
J0944-0038	1.40	-13.07	7.83 ± 0.01	6.89 $^{+0.44}_{-0.25}$	0.16 ± 0.010	2.9 ± 0.1	64 $^{+21}_{-21}$	2.34
J0944+3442	0.69	-15.06	7.62 ± 0.11	8.19 $^{+0.40}_{-0.23}$	0.16 ± 0.013	1.4 ± 0.1	...	3.74
J1016+3754	7.07	-14.43	7.56 ± 0.01	6.77 $^{+0.27}_{-0.22}$	0.07 ± 0.012	4.6 ± 0.2	116 $^{+31}_{-31}$	1.52
J1024+0524	4.50	-18.20	7.84 ± 0.03	7.88 $^{+0.37}_{-0.24}$	0.10 ± 0.016	2.1 ± 0.1	94 $^{+12}_{-12}$	0.40
J1025+3622	1.81	-20.30	8.13 ± 0.01	8.87 $^{+0.25}_{-0.27}$	0.09 ± 0.006	2.4 ± 0.1	155 $^{+24}_{-24}$	0.35
J1044+0353	1.70	-15.25	7.45 ± 0.03	6.84 $^{+0.41}_{-0.26}$	0.08 ± 0.007	6.8 ± 0.1	52 $^{+12}_{-12}$	0.38
J1105+4444	4.68	-17.28	8.23 ± 0.01	8.98 $^{+0.29}_{-0.24}$	0.17 ± 0.005	2.0 ± 0.1	115 $^{+23}_{-23}$	4.11
J1112+5503	1.91	-20.45	8.45 ± 0.06	9.59 $^{+0.33}_{-0.19}$	0.23 ± 0.016	0.9 ± 0.1	349 $^{+107}_{-107}$	0.20
J1119+5130	2.63	-13.54	7.57 ± 0.04	6.81 $^{+0.15}_{-0.28}$	0.10 ± 0.008	2.0 ± 0.1	65 $^{+22}_{-22}$	2.18
J1129+2034	1.87	-13.62	8.28 ± 0.04	8.20 $^{+0.37}_{-0.27}$	0.23 ± 0.011	1.8 ± 0.1	51 $^{+17}_{-17}$	0.38
J1132+5722	2.57	-13.69	7.58 ± 0.08	7.32 $^{+0.23}_{-0.26}$	0.10 ± 0.008	0.8 ± 0.1	...	0.84
J1132+1411	1.75	-15.75	8.25 ± 0.01	8.67 $^{+0.28}_{-0.19}$	0.13 ± 0.008	2.7 ± 0.1	60 $^{+10}_{-10}$	8.86
J1144+4012	1.20	-19.86	8.43 ± 0.20	9.89 $^{+0.18}_{-0.29}$	0.22 ± 0.010	0.6 ± 0.1	246 $^{+33}_{-33}$	0.40
J1148+2546	2.07	-18.03	7.94 ± 0.01	8.13 $^{+0.34}_{-0.24}$	0.10 ± 0.021	3.7 ± 0.1	95 $^{+19}_{-19}$	1.31
J1150+1501	12.60	-13.71	8.14 ± 0.01	6.83 $^{+0.28}_{-0.30}$	0.04 ± 0.004	2.3 ± 0.1	67 $^{+22}_{-22}$	1.29
J1157+3220	14.40	-17.27	8.43 ± 0.02	9.08 $^{+0.32}_{-0.18}$	0.08 ± 0.006	1.2 ± 0.1	238 $^{+49}_{-49}$	2.89
J1200+1343	1.38	-18.53	8.26 ± 0.02	8.12 $^{+0.47}_{-0.42}$	0.15 ± 0.006	5.1 ± 0.1	192 $^{+13}_{-13}$	0.18
J1225+6109	9.50	-13.28	7.97 ± 0.01	7.09 $^{+0.34}_{-0.24}$	0.11 ± 0.005	4.7 ± 0.1	51 $^{+17}_{-17}$	2.91
J1253-0312	9.11	-18.19	8.06 ± 0.01	7.66 $^{+0.51}_{-0.23}$	0.16 ± 0.008	8.0 ± 0.2	113 $^{+38}_{-38}$	0.85
J1314+3452	3.72	-12.65	8.26 ± 0.01	7.53 $^{+0.30}_{-0.21}$	0.14 ± 0.006	2.3 ± 0.1	62 $^{+21}_{-21}$	0.30
J1323-0132	1.33	-15.94	7.71 ± 0.04	6.29 $^{+0.26}_{-0.10}$	0.13 ± 0.042	37.8 ± 3.0	...	0.23
J1359+5726	6.34	-18.53	7.98 ± 0.01	8.39 $^{+0.31}_{-0.26}$	0.09 ± 0.006	2.6 ± 0.1	161 $^{+23}_{-23}$	1.10
J1416+1223	2.62	-20.63	8.53 ± 0.11	9.59 $^{+0.32}_{-0.26}$	0.25 ± 0.008	0.8 ± 0.1	398 $^{+68}_{-68}$	0.13
J1418+2102	1.17	-13.99	7.75 ± 0.02	6.26 $^{+0.49}_{-0.35}$	0.08 ± 0.006	4.7 ± 0.1	51 $^{+7}_{-7}$	0.40
J1428+1653	1.25	-20.75	8.33 ± 0.05	9.56 $^{+0.15}_{-0.23}$	0.14 ± 0.008	1.2 ± 0.1	140 $^{+25}_{-25}$	0.35
J1429+0643	1.62	-20.92	8.10 ± 0.03	8.80 $^{+0.35}_{-0.21}$	0.12 ± 0.012	4.2 ± 0.2	230 $^{+51}_{-51}$	0.15
J1444+4237	2.08	-11.33	7.64 ± 0.02	6.39 $^{+0.17}_{-0.17}$	0.08 ± 0.053	4.1 ± 0.1	54 $^{+18}_{-18}$	8.20
J1448-0110	4.08	-17.55	8.13 ± 0.01	7.58 $^{+0.41}_{-0.24}$	0.15 ± 0.005	8.0 ± 0.1	145 $^{+43}_{-43}$	0.23
J1521+0759	3.52	-20.33	8.31 ± 0.14	9.00 $^{+0.29}_{-0.30}$	0.15 ± 0.008	1.5 ± 0.1	161 $^{+54}_{-54}$	0.28
J1525+0757	3.52	-19.83	8.33 ± 0.04	10.06 $^{+0.28}_{-0.42}$	0.25 ± 0.008	0.5 ± 0.1	408 $^{+28}_{-28}$	0.25
J1545+0858	4.37	-18.40	7.75 ± 0.03	7.50 $^{+0.43}_{-0.26}$	0.11 ± 0.036	8.6 ± 0.3	113 $^{+33}_{-33}$	0.33
J1612+0817	2.70	-21.12	8.18 ± 0.19	9.78 $^{+0.28}_{-0.26}$	0.29 ± 0.008	0.7 ± 0.1	459 $^{+63}_{-63}$	0.20

Note. (1) Object name; (2) UV flux at 1500 Å from Berg et al. (2022); (3) UV absolute magnitude at 1500 Å; (4) metallicity from Berg et al. (2022); (5) stellar mass; (6) dust extinction from Berg et al. (2022); (7) O32 ratio; (8) velocity of Si II absorption line; (9) half-light radius from Xu et al. (2022).

(This table is available in machine-readable form.)

velocity shift, which is not physical. This object is excluded in the following analysis. For completeness, we note that the DLA fit for J1105+4444 failed when constrained by two O I components, and we used a double-Voigt profile with free velocities.

5. The blue part of the J1525+0757 Ly α line is likely a P Cygni profile, so the impact of the geocoronal O I emission should be negligible.
6. We also exclude J1448-0110 from the Ly α emission analysis due to the low S/N.

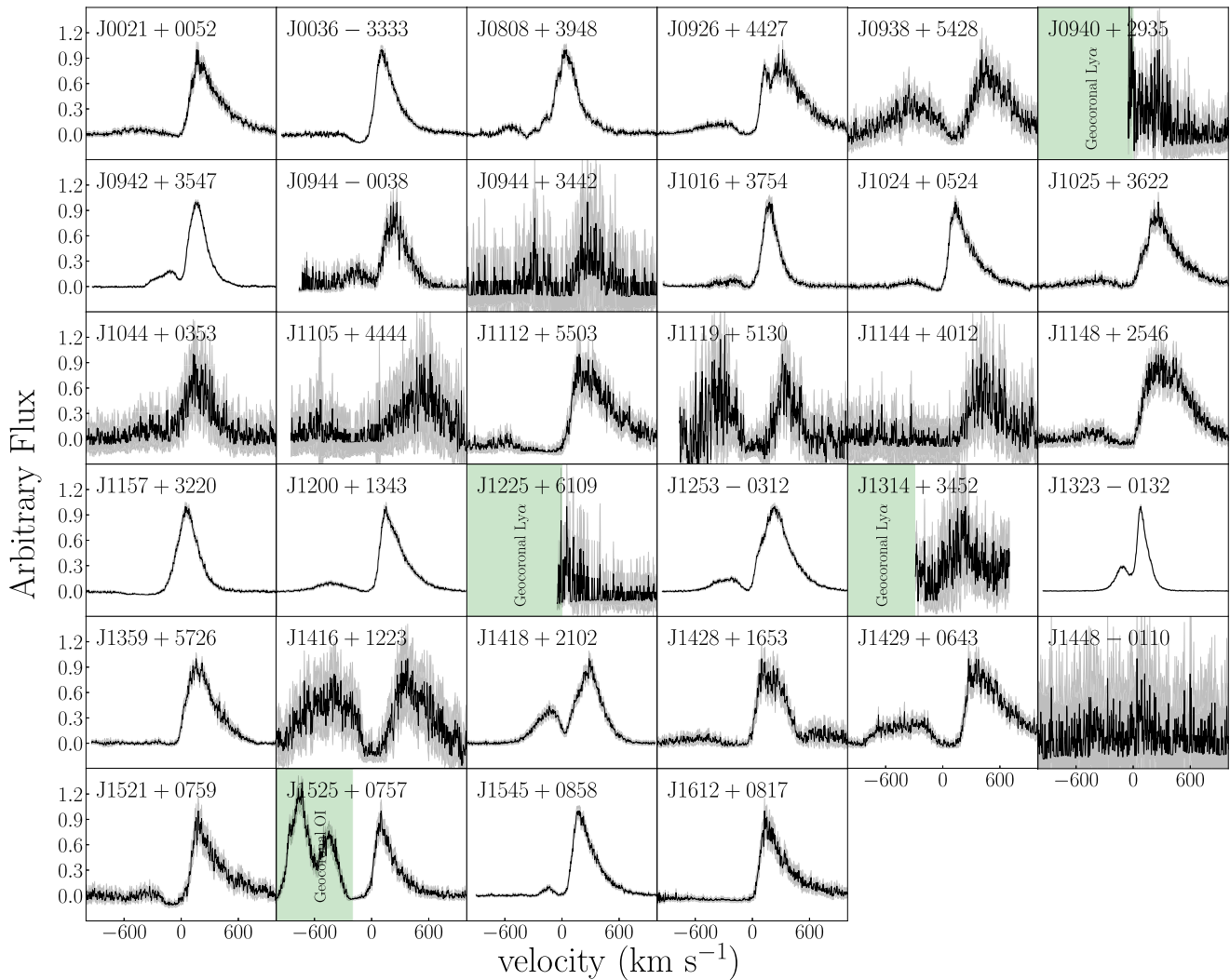


Figure 3. The Ly α spectra (black) and error spectra (gray) after subtracting the continuum and DLA of 34 CLASSY galaxies. We use green shades to show the masked geocoronal Ly α and O I emission lines. The continuum-subtracted spectra are normalized by peak flux. The total Ly α fluxes are measured by integrating fluxes within the wavelength range where Ly α emission lines meet zero flux.

2.2. DLA System and Aperture Loss

The fraction of emitted Ly α photons captured by the 2''5 diameter COS aperture will vary dramatically among the targets because of their large range of distances. For a typical target, the physical diameter of the aperture is roughly 700 pc, which is larger than the half-light radius of the UV continuum emission core but smaller than the Strömgren radius of the nebula.¹⁸ The most distant CLASSY targets are LBAs at $z \approx 0.18$. Here, the COS aperture subtends nearly 8 kpc, vignetting extended halo emission but likely capturing most of the Ly α luminosity. CLASSY also includes several very nearby galaxies, where the COS aperture subtends just a few hundred parsecs, and the damped Ly α absorption troughs are prominent in their spectra (see Figures 1 and 2).

We suggest that the DLA detections indicate the Ly α emission is scattered outside the COS aperture. In support of this claim, Figure 6 shows that 14 of 16 galaxies with UV half-light radii larger than the COS aperture (Xu et al. 2022) have a

DLA in their COS spectrum.¹⁹ The frequency of DLA detections is reduced among the galaxies with half-light radii smaller than the COS aperture. The Lyman break analog sample has the fewest DLA detections. Although the physical size of the aperture grows with increasing redshift, we do not find a one-to-one correlation between DLA detections and redshift. For $z > 0.1$ (yellow circles), the physical scale of COS aperture reaches ~ 5 –10 kpc and is larger than the UV sizes of those galaxies; however, a large fraction (4/9) of their spectra still show significant DLA system. The spectra of high-redshift galaxies observed with similar aperture size sometimes show DLA systems as well (Steidel et al. 2011; Reddy et al. 2016, 2022; Lin et al. 2023). For example, Steidel et al. (2011) reveals a similar fraction (40/92) of galaxies at redshift ~ 2.2 –3.2, which shows the DLA system.

We can gain some quantitative insight from the Ly α imaging studies of Hayes et al. (2014). LARS 9 and LARS 14 correspond to the CLASSY galaxies J0823+2806 at $z = 0.04722$, and J0926+4427 at $z = 0.18067$, respectively.

¹⁸ To estimate the volume ionized by the stars within the COS aperture we have used the extinction corrected the H α luminosity in the SDSS fiber and assumed a volume-average electron density of 1 cm^{-3} and case B recombination at 10^4 K .

¹⁹ The sizes of compact galaxies with $r_{50} < 0''.4$ are measured using COS acquisition images and the sizes of extended galaxies are measured using SDSS u -band images.

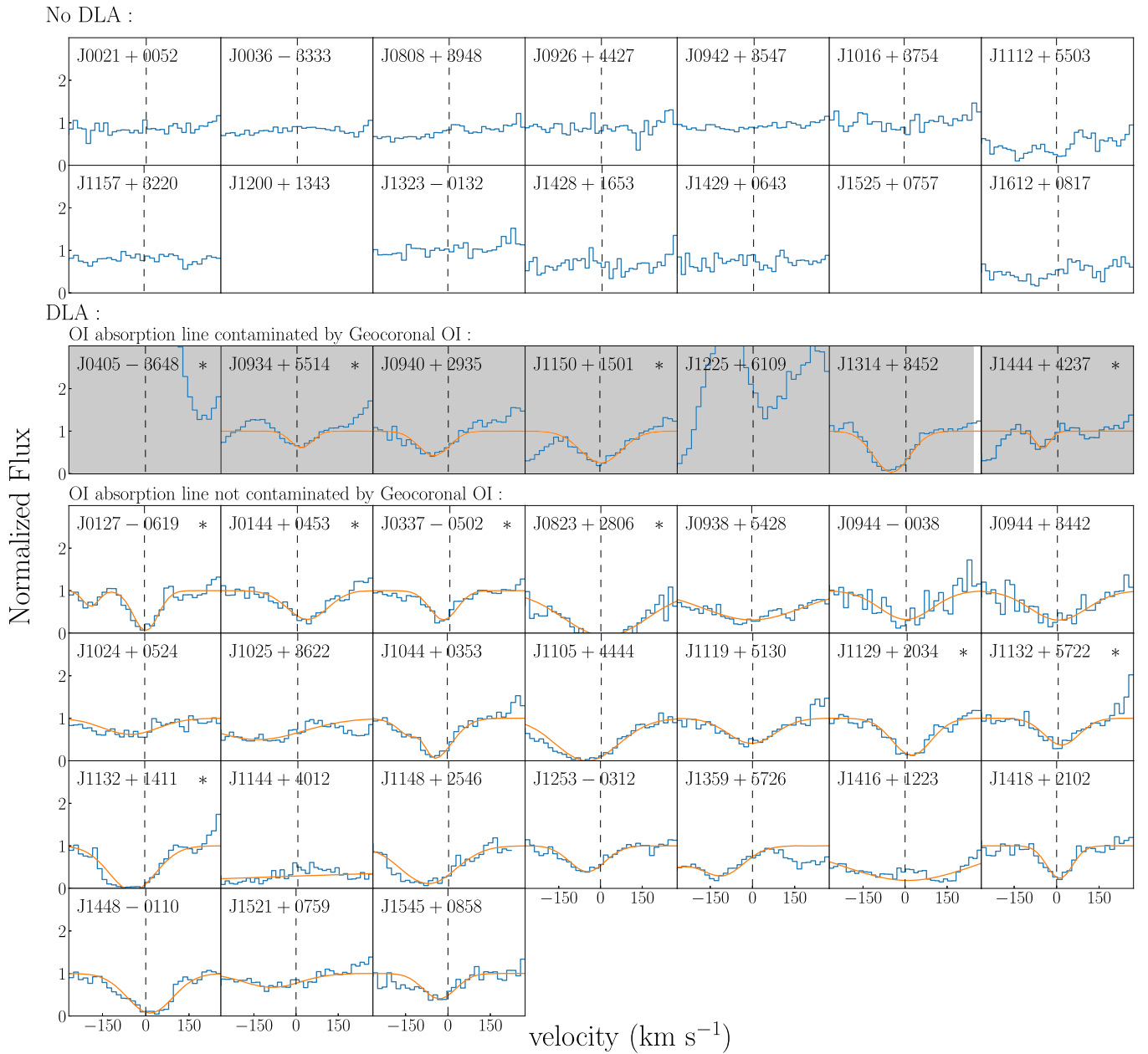


Figure 4. O I absorption profiles (blue) of CLASSY sample. The orange lines indicate best-fit Gaussian profiles. The first two rows show O I absorption profiles of galaxies without DLA system. The third row shows those O I profiles that might overlap with geocoronal O I emission, and the rest shows others. The shaded regions show the wavelength range (1302.2–1307.5 Å) that might be contaminated by geocoronal O I emission lines. An example of geocoronal O I line can be seen in the spectrum of J1525+0757, as shown in the online component of Figure 2. The O I absorption lines of 2 galaxies (J0405-3648 and J1225+6109) overlap with geocoronal O I line; thus, we adopt their C II velocities as DLA velocities. The vertical dashed lines indicate the zero velocity. Asterisks mark galaxies that show a pure DLA system with no Ly α emission.

The closer galaxy shows a pure-DLA Ly α profile, whereas the more distant one has a double-peaked emission profile with no DLA. An inspection of Figure 1 in Hayes et al. (2014) shows the Ly α emission comes from a shell around J0823+2806, whereas the Ly α emission from J0926+4427 is centrally concentrated. In the latter example, the COS aperture includes roughly 60% of the total Ly α flux (Hayes et al. 2014, Figure 4), showing that the Ly α luminosity is significantly attenuated even in the case of no absorption. For the DLA, the growth curve shows net emission only when the aperture is enlarged to a diameter of 9.5 kpc, about 4 times larger than the COS aperture. Galaxy-by-galaxy aperture corrections for Ly α are not currently available, but these examples support our

conjecture that the galaxies showing damped Ly α absorption would show net emission in spectra obtained through larger apertures.

2.3. Ly α Measurements

In this section, we present the measurements of the Ly α emission properties. We measure the continuum and DLA-subtracted profiles. We will demonstrate in Section 3 that the Ly α emission emerges from holes between the DLA clouds. Since these parts of the line profile have different origins, they must be separated to obtain a meaningful analysis.

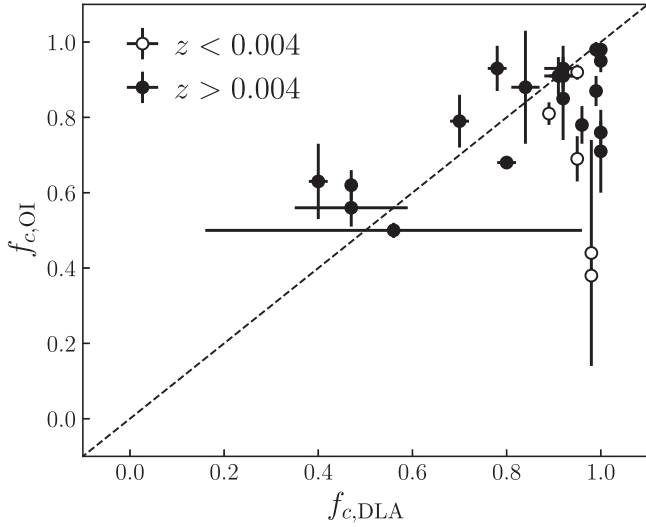


Figure 5. DLA covering fraction vs. O I covering fraction. We mark those O I covering fractions that are possibly contaminated by geocoronal O I emission line (at 1302.2–1307.5 Å) as open circles. Excluding those points, the observed correlation suggests O I covering fraction probe H I covering fraction.

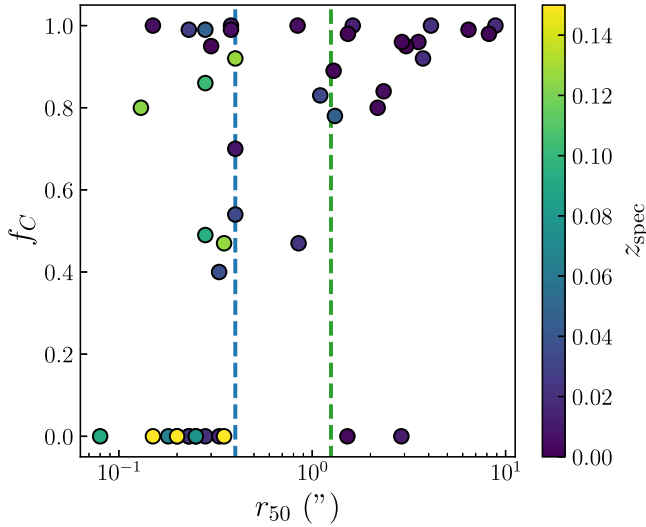


Figure 6. The DLA covering fraction vs. the angular UV half-light radius. A covering fraction of 0 indicates no DLA. We color-coded the circles based on their spectroscopic redshift, thereby identifying variations in the physical scale of the aperture. We also use the blue and green vertical dashed lines to indicate the unvignetted radius ($0''.4$) and the total radius ($1''.25$) for the COS aperture. Roughly a half of higher-redshift galaxies ($z > 0.1$) show significant DLA system. This fraction increases to the lower-redshift sample, which tends to have a larger UV size (in arcsec) due to the projection effect.

2.3.1. Ly α Kinematics

We measure the blue peak velocity, $v_{\text{blue}}^{\text{Ly}\alpha}$, and red peak velocity, $v_{\text{red}}^{\text{Ly}\alpha}$, as the position of the local maximum in the Ly α emission line at velocity $v < 0$ and $v > 0$, respectively, relative to the systemic velocity. The minimum between the two emission peaks defines the Ly α trough velocity, $v_{\text{trough}}^{\text{Ly}\alpha}$. We define the peak separation as $\Delta v_{\text{Ly}\alpha} = v_{\text{red}}^{\text{Ly}\alpha} - v_{\text{blue}}^{\text{Ly}\alpha}$.

2.3.2. Ly α Fluxes and Ly α Escape Fraction

For double-peaked Ly α profiles, we measure the fluxes of the blue and red components by integrating to the velocity of the Ly α trough between the components. We also measure

the asymmetry parameter of the red peak of Ly α emission, defined as $A_f = (\int_{\lambda_{\text{trough}}^{\text{red}}}^{\infty} f_{\lambda} d\lambda) / (\int_{\lambda_{\text{trough}}}^{\lambda_{\text{peak}}^{\text{red}}} f_{\lambda} d\lambda)$, where $\lambda_{\text{peak}}^{\text{red}}$ is the wavelength of the red peak, and λ_{trough} is the wavelength of the trough (Rhoads et al. 2003; Kakiichi & Gronke 2021). The total Ly α fluxes are measured by integrating flux between the wavelengths where the profile meets zero flux, including the central dip in double-peaked profiles and the negative flux in P Cygni profiles. We convert the total Ly α fluxes to luminosity using the luminosity distance from Table 1, which is corrected for the cosmic flow. The rest-frame equivalent widths, EWs, are computed using the Ly α spectra and the *total stellar continuum*, $\text{EW}(\text{Ly}\alpha) = \int F_{\text{Ly}\alpha}(\lambda) / F_{\text{cont}}(\lambda) d\lambda / (1+z)$.

We estimate the Ly α escape fractions $f_{\text{esc}}^{\text{Ly}\alpha}$ based on intrinsic Ly α fluxes inferred through dust-corrected H α (or H β) fluxes assuming a Case B recombination (Brocklehurst 1971): $f_{\text{esc}}^{\text{Ly}\alpha} = F_{\text{Ly}\alpha} / (8.7 \times F_{\text{H}\alpha})$.²⁰ Mingozi et al. (2022) have measured the H α and H β fluxes using optical spectra from SDSS, MUSE, KCWI, MMT, and VIMOS. Since the UV spectra and optical spectra are obtained via different instruments with different aperture sizes, a scaling factor between UV spectra and optical spectra is needed to correct the different aperture losses. Mingozi et al. (2022) measured the scaling factor by matching the optical spectra to the extrapolation of the best-fit UV stellar continuum model (see their Appendix A). The scaling factors for most objects approximate the ratio between apertures of different instruments but are not exactly the same because some other effects may also cause the flux offsets such as the vignetting. For example, the median of the scaling factor for SDSS spectra is ~ 0.79 , and the aperture size ratio is $(2''.5)^2 / (3''.0)^2 \sim 0.69$. We refer readers to Mingozi et al. (2022) for more details. In this work, we adopt the corrected H α fluxes. Since the H α for J0934+5514 and J1253-0312 are unavailable, we convert their H β fluxes to H α fluxes using a factor of 2.86, by assuming Case B recombination with a temperature of 10,000 K and electron density of 100 cm^{-3} .

2.3.3. Ly α Trough Flux Density

The flux density at the Ly α trough velocity defines the trough flux density, f_{trough} . The f_{trough} of J0926+4427 and J1429+0643 have also been measured in Gazagnes et al. (2020) based on the spectra obtained by HST/COS G140L with a resolution of 1500. Gazagnes et al. (2020) measured the Ly α trough flux density based on the continuum-unsubtracted spectra, but our measurements are based on the continuum-subtracted Ly α spectrum. Thus, our $F_{\text{trough}}/F_{\text{cont}}$ should be lower by 1 compared to those in Gazagnes et al. (2020). Here, F_{cont} is the flux density of *total stellar continuum* estimated from STARBURST99.

However, accounting for this difference, the $F_{\text{trough}}/F_{\text{cont}}$ of J0926+4427 and J1429+0643 in our measurements are still lower. In particular, for J0926+4427, we do not see the net residual Ly α trough flux density (i.e., $F_{\text{trough}} < 0$). This is because the CLASSY spectra have much higher resolution, ranging from ~ 2200 to 15,000 with a median of 5000 (measured from MW absorption line; Berg et al. 2022). The high-resolution spectra resolve the small structures at the central trough, which were smoothed due to the lower resolution in Gazagnes et al. (2020). We note that the

²⁰ We adopt the factor of 8.7 to be consistent with previous works. It corresponds to a temperature of 10,000 K and an electron density of $\sim 300 \text{ cm}^{-3}$.

resolution around Ly α emission line might be lower than the resolution for the continuum as Ly α emission, which often subtends a larger solid angle than that of the continuum.

2.3.4. Aperture Effects on Ly α Measurements

The COS aperture, therefore, attenuates the Ly α emission relatively more than the UV emission due to the scattering of Ly α photons. Thus, even though Ly α , H α , and the UV continuum are measured locally in the same aperture, we expect $f_{\text{esc}}^{\text{Ly}\alpha}$ and the Ly α EW to be underestimated. In our example of J0823+2806, see discussion in Section 2.2, the attenuation is severe because most of the Ly α emission is scattered outside the COS aperture. If scattering outside the COS aperture produces the large fraction of DLA systems in CLASSY, then the $f_{\text{esc}}^{\text{Ly}\alpha}$ and Ly α EW of these galaxies are significantly underestimated.

A more subtle bias that we will examine is the possibility that this vignetting modifies the shape of the Ly α emission-line profile. Zheng et al. (2010) predicted that the blue-to-red peak ratio (hereafter B/R ratio) would increase with increasing impact parameters because the front-scattered Ly α photons (blue peak) are closer to the resonance center of the outflowing gas and, thus, tend to be scattered to larger impact parameters, compared with the back-scattered Ly α photons (red peak). Integral field spectroscopy confirms this trend in a few Ly α halos (Erb et al. 2018, 2023). Another possible interpretation is that the average projected outflow velocity decreases with the increasing radius (Li et al. 2022).

3. Radiative Transfer Modeling

The high fraction of DLA systems in CLASSY was not anticipated. More surprising, however, was the discovery of double-peaked Ly α emission in the bottom of the broad absorption profiles. We have drawn attention to an important property of these DLA systems; the high-column density gas only partially covers the continuum source (see Section 2.1). The residual intensity in the continuum-normalized spectra indicates the uncovered fraction of the continuum emission (within the COS aperture). In this section, we explore what continuum is linked to the net Ly α emission profile, the total continuum or the uncovered fraction.

Specifically, we utilize the shell model to fit the Ly α profiles that are normalized by the STARBURST99 continuum or the DLA continuum (hereafter normalized Ly α profile²¹). The model Ly α line profile is computed using the Monte Carlo radiative transfer code tlac (Gronke & Dijkstra 2014; Gronke et al. 2015). This technique has been used to successfully reproduce the observed profiles of Ly α emission lines (e.g., Yang et al. 2017; Orlitová et al. 2018; Gurung-López et al. 2022). The shell model can produce Ly α emission when the dust optical depth is low, or a DLA system when there is a substantial neutral hydrogen column with a moderate dust optical depth (e.g., see Figure 1 of Gronke et al. 2015). However, the homogeneous shell model cannot produce a Ly α emission line in the DLA trough, i.e., the Abs+Em profiles seen in our CLASSY sample (see Figure 2). The Ly α emission

line requires low- N_{HI} channels (with low dust optical depth), which contradicts the presence of damped absorption, which requires very-high-column density. This requires a nonuniform shell model to describe the multicomponent ISM. Although radiative transfer through clumpy media has been explored (Hansen & Oh 2006; Verhamme et al. 2015; Gronke et al. 2016, 2017; Li & Gronke 2022), a nonuniform shell is beyond the scope of this work.

Here, we adopt an alternative method to fit the Ly α profiles of the CLASSY sample. We fit and remove the DLA system to extract the net Ly α profile, as described in Section 2.1, and then, we fit the tlac model to the normalized Ly α profile using two different approaches described in Section 3.2. The variant fitting results could reveal the physical links between the gasses probed by Ly α emission and DLA absorption, as discussed in Section 3.2.3.

Some properties of the shell model have been mapped to those of more realistic outflows (Gronke et al. 2016; Li & Gronke 2022). However, the shell-model parameters are found to have systematic discrepancies with independently measured outflow velocities and the velocity dispersion of the intrinsic line profile (e.g., Orlitová et al. 2018). To understand the origin of the discrepancies, we perform more fittings with constrained redshift priors and compare it with the previous results in Section 3.3.

3.1. Shell Model

tlac computes Ly α resonant scattering through a uniform, expanding shell, which is composed of dust and neutral hydrogen gas. The shell model used in tlac has 6 free parameters, including 2 parameters for the central radiation source: intrinsic line width σ_i and intrinsic equivalent width EW_i ; and 4 parameters for the expanding shell (neutral hydrogen column density N_{HI} , dust optical depth τ_d , shell velocity v_{exp} , and temperature T). In addition to these six parameters, a redshift parameter z_{tlac} is also applied to shift the rest frame of the Ly α profile relative to the systemic redshift of the galaxy.

The Ly α photons and underlying continuum photons are generated from the central source with an intrinsic width of σ_i and intrinsic equivalent width of EW_i . The photon is then emitted into the HI shell with a random direction and travels a distance before being absorbed or resonantly scattered. The distance that a photon can travel is calculated using the total optical depth of dust τ_d and neutral hydrogen N_{HI} in the expanding shell with velocity v_{exp} and temperature T . The probability that a photon is resonantly scattered or absorbed at a specific position is estimated by comparing the optical depth of neutral hydrogen with the total optical depth at that position. If the photon is resonantly scattered, a new direction and a new frequency are drawn from the proper phase function and the frequency redistribution function, respectively. The previous steps are repeated until the photon escapes from the simulation domain or is absorbed by the dust. If the photons escape from the simulation domain, their frequency, and other properties are recorded. This simulation has been run thousands of times over a discrete grid of $(v_{\text{exp}}, N_{\text{HI}}, T)$ and then been post-processed with a continuous grid of $(\sigma_i, \tau_d, \text{EW}_i)$ to generate the simulated Ly α spectra for different parameter values. To fit the observed Ly α spectrum, a likelihood function is constructed based on the noise and flux spectra. The best-fit spectrum is derived by maximizing the likelihood function using the

²¹ To avoid confusion, we define the emergent Ly α profile as the observed Ly α emission line with the underlying continuum and DLA, the net Ly α profile as the Ly α profile after removing the underlying continuum and DLA, and the normalized Ly α profile as the net Ly α profile after being normalized by the underlying continuum.

Markov Chain Monte Carlo and nonlinear optimization methods.

We highlight the importance of the intrinsic Ly α equivalent width (EW $_i$) in the shell model, a parameter excluded by studies that fit the continuum-subtracted Ly α line profiles, because the continuum photons are also involved in resonant scattering and can dominate the normalized Ly α profile for low-EW $_i$ cases.

3.2. Profile Fitting

Our profile-fitting approach draws attention to ambiguity about the appropriate continuum level for normalization. When a DLA system is present in the spectrum, the underlying continuum could be the total stellar continuum (red lines in panel (a) of Figure 2), and thus, the normalized spectrum is as follows:

$$I_{\lambda}^{\text{EW}} = (f_{\lambda}^{\text{Ly}\alpha} + f_{\lambda}^{\text{cont}}) / (f_{\lambda}^{\text{cont}}), \quad (3)$$

or the residual stellar continuum in the bottom of DLA system (red line in panel (b)). And thus, the normalized spectrum is as follows:

$$I_{\lambda}^{\text{EW}} = (f_{\lambda}^{\text{Ly}\alpha} + f_{\lambda}^{\text{cont}} \times (1 - f_C)) / (f_{\lambda}^{\text{cont}} \times (1 - f_C)), \quad (4)$$

where $f_{\lambda}^{\text{Ly}\alpha}$ is the Ly α emission line, $f_{\lambda}^{\text{cont}}$ is the best-fit total stellar continuum (see Section 2), and f_C is the covering fraction of DLA system. The choice of the underlying continuum will change the equivalent width of the Ly α line and, thus, the contribution of continuum photons on the emergent Ly α profile. Here, we perform profile fittings, assuming each continuum level in turn, and then discuss the results. We present the best-fit spectra in Appendix. We also present the best-fit model parameters of the second profile fitting in Table 4.

The fitted parameters somewhat degenerate with each other. For example, in the case of outflowing shells, Li & Gronke (2022) demonstrate that various combinations of shell velocity, column density, temperature, and redshift can produce very similar line profiles, for example, (v_{exp} , $\log N_{\text{H I}}$, $\log T$, 0), and $\sim(2v_{\text{exp}}$, $\log N_{\text{H I}} - 0.5$ dex, $\log T + 1$ dex, Δv). Nonetheless, the spectra generated by these parameters show clear differences at the red peak, and our high-S/N spectra should be able to distinguish between the degeneracies.

3.2.1. First Attempt: Total Stellar Continuum

Overall, the quality of the first fitting using the total stellar continuum (Equation (3)) is quite good, given the simplicity of the model. However, in a subset of spectra, the results are unsatisfactory, especially J0938+5428, J0944+3442, J1044+0353, J1119+5130, J1144+4012, J1416+1223, J1521+0759, as presented in Figure 18, of which the best-fit spectra show a very sharp dip around zero velocity compared to the observed Ly α profile.

Looking at their original spectra (see Figure 2), we find that all these poorly fitted Ly α profiles correspond to spectra that show significant DLA systems compared with the successful sample. This result motivated us to investigate whether the sharp dips might be caused by an inappropriate underlying continuum, which underestimated the Ly α EW spectra I_{λ}^{EW} . Thus, we performed a second profile fitting using the residual stellar continuum as described by Equation (4).

3.2.2. Second Attempt: Residual Stellar Continuum

In Figure 19, we present the best-fit t_lac models for Ly α profiles normalized by the residual stellar continua ($1 - f_C$). For the unsatisfactory sample in the first attempt, normalizing the Ly α spectra by the residual stellar continuum significantly improved the best-fit results. The sharp dips seen in the models of Section 3.2.1 no longer exist in the new model spectra. In Figure 7, we compare the reduced χ^2 for the first and second attempts. Clearly, most results are significantly improved if adopting the normalization of the residual stellar continuum. Thus, we can conclude that the dip was caused by an inappropriate continuum level. In further analysis, the first attempt of fitting will not be considered.

For the galaxies without DLA systems, $f_C = 0$, the residual continuum rises to the level of the total continuum. It is therefore not surprising that every Ly α profile is successfully fitted when the residual continuum is used. We conclude that the residual continuum, $1 - f_C$, is the more physical normalization for the emergent Ly α emission line. In other words, the DLA covering fraction f_C gives a good indication of the fraction of the intrinsic Ly α emission that is blocked by the high-column density clouds.

3.2.3. Implication: Scattering Outside COS Aperture Reveals Low- $N_{\text{H I}}$ Channels

We have shown that successful radiative transfer modeling of CLASSY Ly α spectra, in the context of the shell model, requires (1) separating the Ly α emission profile from the DLA system, and (2) normalizing the Ly α emission by the leaked continuum, i.e., the residual flux in the DLA system. This approach divides the COS aperture into two groups of sightlines, hereafter channels, distinguished by their column density. In the schematic picture of a thin shell, these two channels represent clouds and the intercloud medium. More generally, for the targets with $C_f > 0$, the Ly α photons entering the high- $N_{\text{H I}}$ channel do not emerge from the galaxy at radii within the COS aperture. If they did, then the best continuum normalization would be the total stellar continuum, which is inconsistent with our fitting results.

The Ly α photons entering the high- $N_{\text{H I}}$ channel must be scattered to radii larger than the COS aperture before they escape. The alternative is that they are absorbed by dust grains, which seems less likely for two reasons. Most CLASSY galaxies whose COS spectra detect DLA systems have low metallicities and are relatively dust poor. In addition, substantial amounts of dust in the scattering clouds would boost the transmitted Ly α equivalent width (Hansen & Oh 2006), but we do not measure unusually large EW.

When the Ly α emission is separated from the DLA system, what do the shell-model parameters fitted to the emission component represent? Perhaps, the line photons entering low- $N_{\text{H I}}$ channels scatter off both the low $N_{\text{H I}}$ clouds and the walls of the DLA channels. In the limit of no intercloud medium, the kinematics of the dense clouds would determine the shape of the Ly α line profile (Neufeld 1990; Hansen & Oh 2006), so we might expect the kinematics of both the low- and high- $N_{\text{H I}}$ channels to impact the Ly α profile. If Ly α photons entering DLA sightlines are scattered outside the spectroscopic aperture, then the vignetted apertures may have one advantage, namely providing a direct view of the properties in low- $N_{\text{H I}}$ channels.

Table 4
Best-fit Parameters of the Second Attempt

Object	z_{tlac}	v_{exp} (km s^{-1})	$\log N_{\text{HI}}$	$\log T$ (K)	$\log \tau$	σ_i (km s^{-1})	EW_i (\AA)
(1)	(2)	(3)	(4)	(5)	(6)	(7)	(8)
J0021+0052	0.098902	214^{+1}_{-2}	$18.79^{+0.11}_{-0.08}$	$3.8^{+0.2}_{-0.1}$	$-2.05^{+1.01}_{-0.11}$	117^{+1}_{-1}	$16.8^{+0.8}_{-0.7}$
J0036-3333	0.020939	207^{+2}_{-1}	$18.68^{+0.09}_{-0.06}$	$3.5^{+0.2}_{-0.1}$	$-2.10^{+1.13}_{-0.06}$	93^{+1}_{-1}	$6.6^{+0.5}_{-0.1}$
J0808+3948	0.091384	365^{+1}_{-1}	$16.76^{+0.08}_{-0.04}$	$3.4^{+0.1}_{-0.1}$	$-1.57^{+0.22}_{-0.11}$	103^{+1}_{-1}	$8.7^{+0.1}_{-0.1}$
J0926+4427	0.180817	131^{+2}_{-3}	$19.23^{+0.05}_{-0.08}$	$3.7^{+0.1}_{-0.1}$	$-1.74^{+0.11}_{-0.21}$	248^{+2}_{-3}	$31.8^{+1.0}_{-1.0}$
J0938+5428	0.102513	21^{+4}_{-2}	$19.79^{+0.08}_{-0.08}$	$4.2^{+0.2}_{-0.1}$	$-0.68^{+0.74}_{-0.87}$	308^{+5}_{-4}	$74.5^{+5.3}_{-4.4}$
J0942+3547	0.015121	86^{+1}_{-1}	$18.20^{+0.06}_{-0.06}$	$3.1^{+0.1}_{-0.1}$	$-3.31^{+0.38}_{-0.09}$	167^{+1}_{-1}	$18.3^{+0.1}_{-0.1}$
J0944-0038	0.005187	119^{+4}_{-4}	$18.60^{+0.09}_{-0.07}$	$3.4^{+0.2}_{-0.2}$	$-1.35^{+0.20}_{-0.12}$	218^{+3}_{-4}	$2130.2^{+1851.2}_{-1159.2}$
J0944+3442	0.020226	72^{+18}_{-17}	$19.44^{+0.21}_{-0.23}$	$4.1^{+0.7}_{-0.8}$	$0.44^{+0.46}_{-0.43}$	182^{+12}_{-11}	$39.6^{+21.4}_{-14.0}$
J1016+3754	0.004131	96^{+2}_{-1}	$18.85^{+0.07}_{-0.11}$	$4.3^{+0.1}_{-0.2}$	$0.10^{+0.80}_{-0.75}$	142^{+1}_{-2}	$26.2^{+1.9}_{-1.9}$
J1024+0524	0.033425	176^{+2}_{-1}	$19.01^{+0.08}_{-0.09}$	$5.1^{+0.1}_{-0.2}$	$-1.89^{+0.92}_{-0.16}$	82^{+1}_{-1}	$16.2^{+0.6}_{-0.4}$
J1025+3622	0.126786	167^{+3}_{-2}	$18.99^{+0.09}_{-0.07}$	$4.2^{+0.2}_{-0.1}$	$-0.88^{+0.40}_{-0.55}$	245^{+3}_{-3}	$41.3^{+2.1}_{-1.9}$
J1044+0353	0.013070	175^{+10}_{-15}	$18.18^{+0.20}_{-0.19}$	$3.5^{+0.3}_{-0.4}$	$-1.14^{+0.25}_{-0.10}$	248^{+14}_{-9}	$9.9^{+0.9}_{-0.7}$
J1112+5503	0.131707	210^{+3}_{-3}	$19.55^{+0.10}_{-0.05}$	$4.6^{+0.3}_{-0.1}$	$0.55^{+1.10}_{-1.17}$	270^{+3}_{-4}	$20.9^{+1.5}_{-1.6}$
J1119+5130	0.004536	0^{+2}_{-1}	$20.42^{+0.24}_{-0.65}$	$4.0^{+0.4}_{-0.3}$	$-1.80^{+1.21}_{-0.03}$	316^{+10}_{-8}	$6.5^{+6.6}_{-2.4}$
J1144+4012	0.126832	108^{+11}_{-8}	$20.20^{+0.07}_{-0.08}$	$4.9^{+0.3}_{-0.7}$	$0.40^{+0.46}_{-0.52}$	259^{+9}_{-11}	$281.6^{+50.7}_{-41.7}$
J1148+2546	0.045710	279^{+5}_{-4}	$19.19^{+0.09}_{-0.07}$	$3.8^{+0.2}_{-0.2}$	$0.53^{+0.67}_{-0.56}$	281^{+4}_{-4}	$46.3^{+3.7}_{-3.6}$
J1157+3220	0.010230	163^{+1}_{-2}	$20.06^{+0.04}_{-0.09}$	$5.0^{+0.1}_{-0.2}$	$0.69^{+1.98}_{-1.60}$	191^{+1}_{-2}	$200.1^{+2.7}_{-3.5}$
J1200+1343	0.066942	173^{+1}_{-2}	$16.56^{+0.09}_{-0.05}$	$5.4^{+0.1}_{-0.1}$	$-2.40^{+0.65}_{-0.12}$	266^{+1}_{-1}	$53.6^{+1.7}_{-1.8}$
J1253-0312	0.023087	184^{+0}_{-1}	$18.67^{+0.03}_{-0.06}$	$4.3^{+0.1}_{-0.1}$	$-2.70^{+0.48}_{-0.00}$	256^{+1}_{-1}	$31.7^{+0.5}_{-0.4}$
J1323-0132	0.022534	37^{+1}_{-1}	$17.93^{+0.05}_{-0.02}$	$3.1^{+0.0}_{-0.1}$	$-2.40^{+0.24}_{-0.12}$	121^{+0}_{-0}	$75.7^{+1.1}_{-1.1}$
J1359+5726	0.034107	205^{+2}_{-1}	$19.03^{+0.13}_{-0.09}$	$4.7^{+0.1}_{-0.2}$	$-1.11^{+0.10}_{-0.47}$	128^{+2}_{-2}	$51.8^{+2.5}_{-2.2}$
J1416+1223	0.123181	0^{+2}_{-2}	$19.59^{+0.09}_{-0.08}$	$4.6^{+0.2}_{-0.3}$	$-0.22^{+0.70}_{-0.73}$	289^{+6}_{-6}	$49.5^{+4.1}_{-3.9}$
J1418+2102	0.009016	98^{+2}_{-2}	$18.18^{+0.09}_{-0.06}$	$3.0^{+0.1}_{-0.1}$	$0.68^{+1.65}_{-1.61}$	230^{+1}_{-1}	$101.8^{+4.8}_{-4.9}$
J1428+1653	0.181780	121^{+3}_{-4}	$18.80^{+0.10}_{-0.07}$	$3.5^{+0.1}_{-0.2}$	$-1.12^{+0.08}_{-0.40}$	52^{+1}_{-1}	$17.8^{+1.9}_{-1.0}$
J1429+0643	0.173984	112^{+2}_{-3}	$19.21^{+0.08}_{-0.09}$	$3.1^{+0.2}_{-0.2}$	$-0.38^{+0.67}_{-0.82}$	323^{+5}_{-5}	$46.8^{+3.6}_{-3.1}$
J1521+0759	0.094771	215^{+2}_{-2}	$19.08^{+0.12}_{-0.11}$	$3.0^{+0.2}_{-0.1}$	$-1.04^{+0.16}_{-0.28}$	93^{+2}_{-2}	$9.2^{+1.8}_{-0.6}$
J1525+0757	0.075913	136^{+2}_{-1}	$18.58^{+0.09}_{-0.06}$	$4.5^{+0.2}_{-0.1}$	$-1.39^{+0.00}_{-0.44}$	52^{+1}_{-1}	$19.2^{+1.2}_{-1.0}$
J1545+0858	0.038336	194^{+1}_{-1}	$18.41^{+0.07}_{-0.10}$	$3.0^{+0.2}_{-0.1}$	$0.69^{+1.91}_{-1.88}$	156^{+1}_{-1}	$55.3^{+1.5}_{-1.8}$
J1612+0817	0.149267	246^{+3}_{-2}	$19.61^{+0.08}_{-0.10}$	$5.3^{+0.2}_{-0.2}$	$0.09^{+1.03}_{-1.11}$	112^{+2}_{-2}	$35.6^{+2.3}_{-2.0}$

Note. (1) Object name; (2) redshift estimated by the shell model; (3) outflow velocity of expanding shell; (4) H I column density; (5) temperature; (6) dust extinction; (7) intrinsic line width; (8) equivalent width.

(This table is available in machine-readable form.)

3.3. Discrepancies between the Shell Model and Observations

We have presented that whether the shell model can well-fit the observed Ly α profile is critical to infer the ISM properties. However, the three discrepancies reported in Orlitova et al. (2018; see also Section 1) might suggest a limited physical meaning of the model parameters. These discrepancies are also observed in the CLASSY sample with high significance, as shown in Figure 8 (black circles). The best-fit redshifts are always larger by 0–200 km s^{-1} than the spectroscopic redshift, consistent with Orlitova et al. (2018). One possible origin of the discrepancies is the degeneracies between the model parameters, suggested in Li & Gronke (2022). To test this scenario and gain more insight into the discrepancies, we perform a third profile fitting following Li & Gronke (2022), which constrains the range of redshift parameters to break the degeneracies.

3.3.1. Third Attempt: Constraining the Redshift

The CLASSY redshifts derived from UV nebular lines agree well with those derived from optical lines; the standard deviation of velocity difference is $\sim 22 \text{ km s}^{-1}$

(Mingozzi et al. 2022). A spatial offset between the scattered Ly α emission and the optically thin emission lines would introduce an additional redshift error if, and only if, the offset were along the dispersion axis of the spectrograph. Based on the radius of the unvignetted aperture ($0''.4$), a nonperfect alignment could shift the Ly α wavelength scale by as much as $\pm 44 \text{ km s}^{-1}$. For a redshift-constrained fit, we adopted a narrow Tophat probability distribution of width $\pm 44 \text{ km s}^{-1}$ as the prior on redshift. The best-fit spectra are presented in Figure 9. In contrast, in the second attempt at profile fitting (Section 3.2.2), we adopted a Gaussian prior on redshift, and this broad distribution with $\sigma(z_{\text{tlac}}) = 120 \text{ km s}^{-1}$ serves as the unconstrained fit.

3.3.2. Can Constrained Fitting Alleviate the Discrepancies?

The redshift differences are apparently improved when adopting the constrained fitting (red circles in Figure 8). This is because the constrained redshift prior sets a hard limit of the difference to be 44 km s^{-1} . On the other hand, comparing the best-fit Ly α profiles of the constrained fitting (see Figure 9) with those of the unconstrained fitting (see Figure 19), it is hard

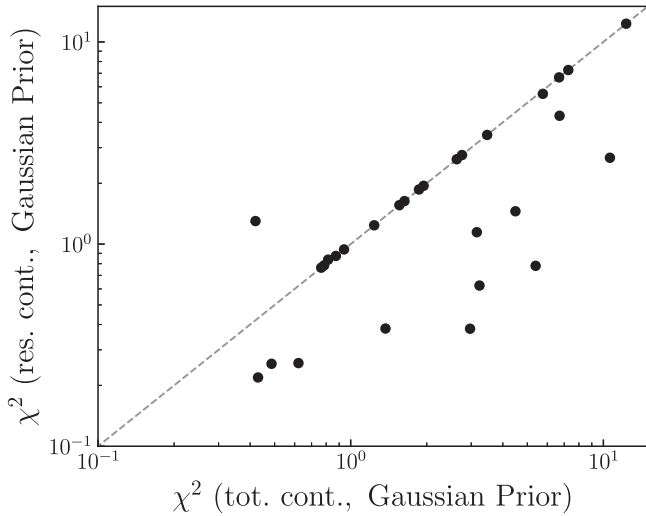


Figure 7. Reduced χ^2 values of best-fit Ly α profiles derived by the first attempt of profile fitting (using total stellar continuum and Gaussian redshift prior) and the second attempt of profile fitting (using residual stellar continuum and Gaussian redshift prior). We notice that, except for one object (J0944-0038), the fitting results for objects with DLA are significantly improved if adopting the residual continua, which are corrected for the DLA covering fraction $(1 - f_c)$. For objects without DLA, the corrected continuum equals to the total stellar continuum. Thus, the reduced χ^2 does not change. We note the reduced χ^2 of some galaxies (J0944+3442, J1044+0353, J1144+4012, J1148+2546, J1416+1223) are much smaller than unity. This might be due to their error spectra being overestimated (comparing to their flux fluctuation, see Figure 3).

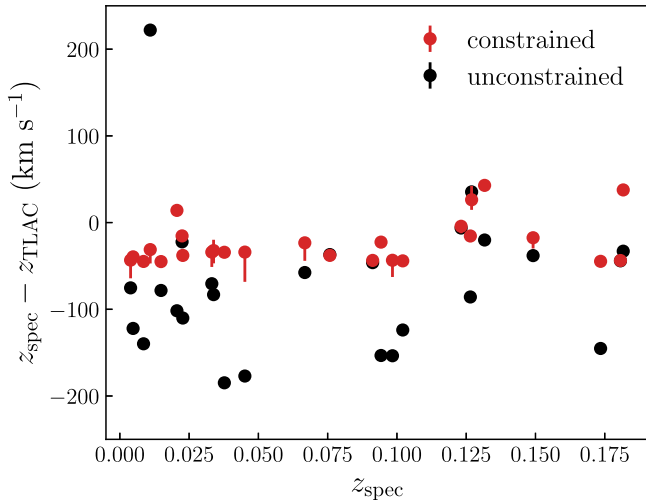


Figure 8. Redshift difference between tLAC redshift z_{tLAC} and spectroscopic redshift z_{spec} . The black circles indicate the results of the second attempt of profile fitting with a Gaussian prior with $\sigma = 120 \text{ km s}^{-1}$ for redshift (unconstrained fitting). The red circles indicate the results of the third attempt of profile fitting with a Tophat prior with a width of $\pm 44 \text{ km s}^{-1}$ for redshift (constrained fitting).

to distinguish the difference between them by visual inspection. We compare the reduced χ^2 of two profile fittings in Figure 10, which shows that the results of constrained profile fitting are slightly worse than those of unconstrained profile fitting, but still acceptable.²² Thus, our test confirms that adopting a

²² We notice two best-fit spectra (J1112+5503, J1323-0132) of constrained profile fitting are improved compared with the unconstrained profile fitting. This might be because the unconstrained profile fitting for these two objects is trapped in a local maximum of the likelihood.

constrained redshift prior for the profile fitting can somewhat alleviate the redshift discrepancy observed in previous works (Yang et al. 2016; Orlitová et al. 2018). We present the best-fit parameters of the third profile fitting in Table 5.

However, the best-fit redshift remains systematically larger than the spectroscopic redshift as most of the red circles are still below zero velocity. This indicates that the constrained fitting does not fully resolve the observed discrepancies. We return to this topic in Section 4.3.3, where we combine the comparison between the tLAC shell velocity and spectral measurements of outflow velocity.

We do not discuss the line width discrepancy in this work because a clumpy model is needed to resolve this discrepancy. By comparing the Ly α profiles generated by the uniform shell model and a clumpy model, Gronke et al. (2017), Li & Gronke (2022) find that a larger line width is always required for the shell model to produce a similar Ly α profile as that from the clumpy model. The intrinsic difference between the two models is that the clumpy model includes the turbulent velocity dispersion of the clumps while the shell model does not. Thus, the line width of the shell model needs to be artificially broadened to compensate for the omission of turbulent motion in the shell model.

4. Properties of the Neutral ISM

In this section, we discuss the relationship between the HI column densities inferred from the Ly α absorption and emission components of the line profile. We then discuss indirect evidence LyC leakage. Finally, we return to the problem of why the shell model systematically misrepresents outflow properties, finding that the problem lies in the spectroscopic aperture.

4.1. Structure of the ISM in CLASSY Galaxies

In Section 3, we found evidence that the neutral ISM consists of several components with different column densities. The DLA system requires high- N_{HI} clouds with $N_{\text{HI}} > 10^{20} \text{ cm}^{-2}$. In Section 3.2, the tLAC fitting revealed that the observed Ly α emission line requires low- N_{HI} holes with $10^{18} < N_{\text{HI}} < 10^{20} \text{ cm}^{-2}$. Combining these two results demonstrates the existence of sightlines with different HI column densities in individual galaxies. We have argued that the scattering of a significant fraction of the Ly α photons out of the COS aperture makes the high- N_{HI} channels visible via Ly α absorption, whereas their damping profiles would be filled in by scattered emission in spectra obtained through larger apertures. Apparently, the Ly α halos of many CLASSY galaxies are much larger than the COS aperture, and the scattering of Ly α photons out of the COS aperture provides a unique opportunity to describe the structure of the neutral ISM, as we show here.

New insight into how LyC radiation escapes from local analogs of EoR galaxies may be obtained by comparing the structure of the ISM in hydrodynamical simulations to the column density distribution we derive. Feedback from massive stars is widely believed to shape the pathways for LyC escape, but the mechanism is debated. For example, Ma et al. (2020) argue that positive feedback, essentially propagating star formation triggered by the mechanical feedback from massive stars, is essential to shift the production of LyC radiation away from the densest region of a galaxy. In contrast, in H II regions too young to have produced supernova explosions, the

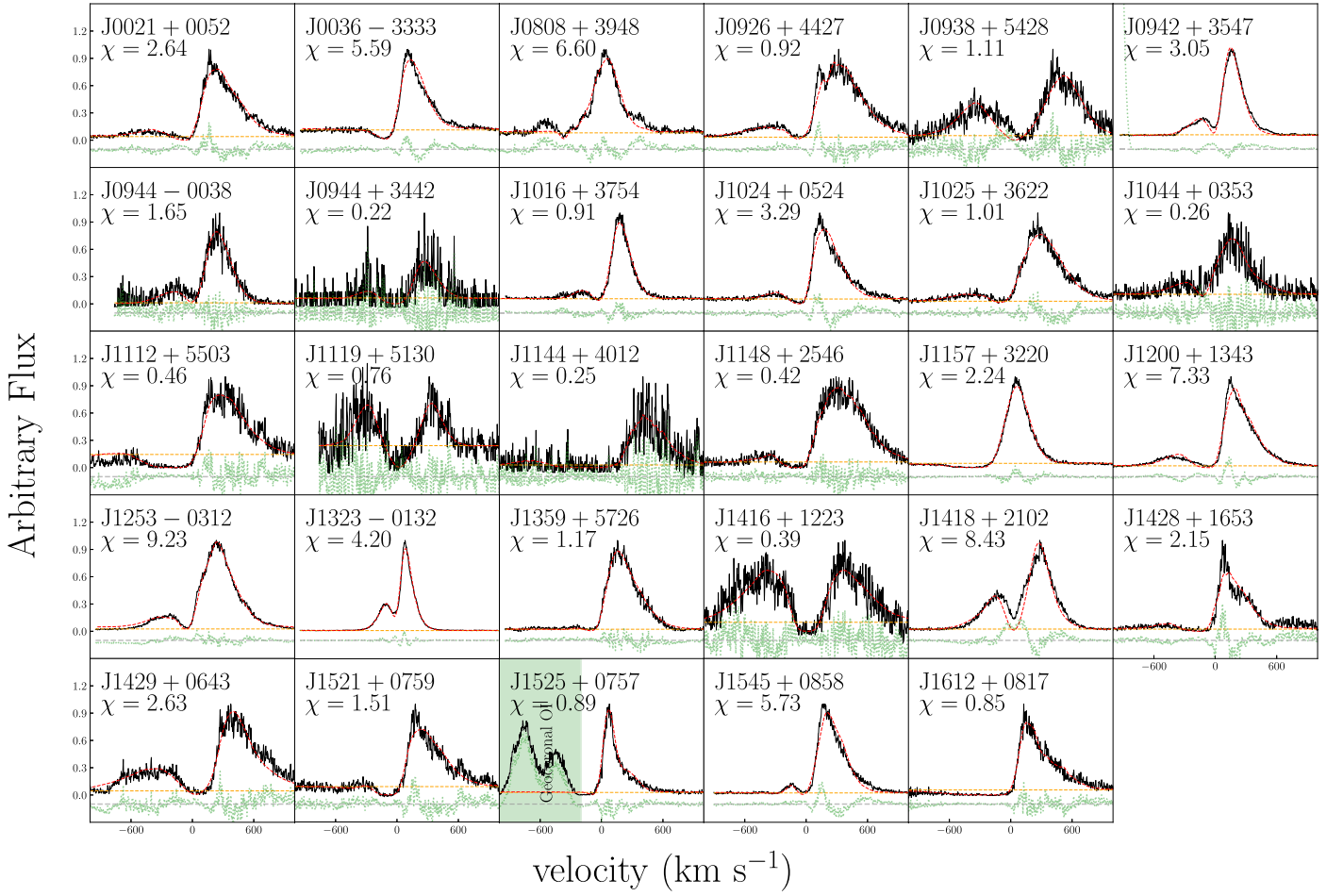


Figure 9. Best-fit Ly α spectra (red) for 29 CLASSY galaxies using the residual stellar continuum and a Tophat redshift prior with a width of ± 48 km s $^{-1}$ (third attempt). The spectra are normalized by the peak flux, and the orange dashed lines indicate the continuum level for each object. We use the green lines to show the residual and manually shift it by -0.1 for better illustration. The gray dashed lines indicate the zero level of the residual.

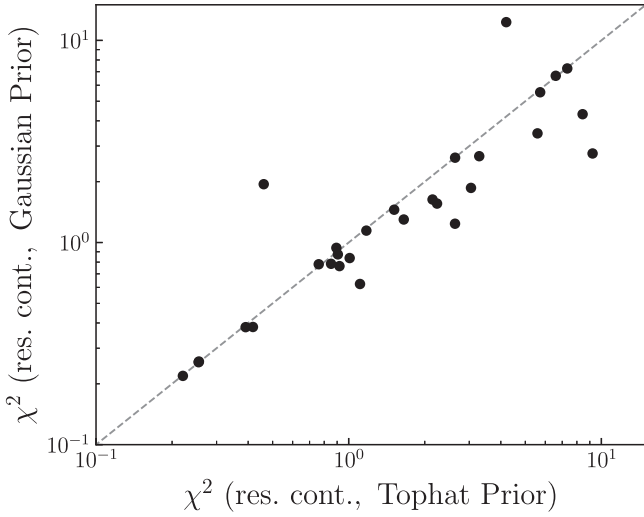


Figure 10. Reduced χ^2 values of best-fit Ly α profiles derived by the second attempt (using the residual continuum and a Gaussian redshift prior) and the third attempt (using the residual continuum and a Tophat redshift prior). The second attempt adopts a Gaussian probability distribution with σ of 120 km s $^{-1}$ as prior, and the third attempt adopts a Tophat probability distribution with a width of ± 48 km s $^{-1}$ as prior.

turbulence driven by ionization fronts may open channels for LyC escape (Kakiichi & Gronke 2021).

One difference between these two mechanisms is the size of the channels. Whereas the channels opened by turbulence are individually small, the low- N_{HI} bubbles driven by mechanical feedback have scales reaching hundreds of parsecs (Ma et al. 2020). Thus, the size of the channels provides insight of particular interest for understanding the escape pathways.

In this section, we adopt the column density estimation from the third profile fitting (see Section 3.3), because it incorporates more constraints from the observation. However, adopting the estimation from the second profile fitting does not change the conclusion of this section.

4.1.1. Column Density Distribution of Neutral ISM

Figure 11 compares the distribution of low- N_{HI} channels returned by the shell-model fits and the high- N_{HI} column densities measured from the damping wing absorption. In the top panel, the histograms are normalized by the total number of galaxies showing a DLA system or Ly α emission line, respectively. Their combined distribution has two peaks: one at $N_{\text{HI}} \approx 10^{19}$ cm $^{-2}$, which represents the path of the escaping Ly α photons,²³ and a second peak representing the typical

²³ If adopting the N_{HI} from the second profile fitting, the peak shifts to lower by 0.4 dex.

Table 5
Best-fit Parameters of the Third Attempt

Object	z_{tlac}	v_{exp} (km s^{-1})	$\log N_{\text{HI}}$	$\log T$ (K)	$\log \tau$	σ_i (km s^{-1})	EW_i (\AA)
(1)	(2)	(3)	(4)	(5)	(6)	(7)	(8)
J0021+0052	0.098535	163_{-2}^{+1}	$19.17_{-0.05}^{+0.16}$	$4.5_{-0.1}^{+0.2}$	$-0.67_{-0.07}^{+0.19}$	225_{-1}^{+1}	$26.7_{-1.1}^{+4.0}$
J0036-3333	0.020553	120_{-2}^{+2}	$19.17_{-0.05}^{+0.08}$	$3.0_{-0.1}^{+0.1}$	$-0.63_{-0.04}^{+0.04}$	142_{-2}^{+2}	$9.0_{-0.3}^{+0.3}$
J0808+3948	0.091375	348_{-2}^{+2}	$16.17_{-0.05}^{+0.08}$	$3.7_{-0.1}^{+0.1}$	$-1.67_{-0.73}^{+0.46}$	102_{-1}^{+1}	$8.7_{-0.1}^{+0.1}$
J0926+4427	0.180816	133_{-1}^{+1}	$19.19_{-0.06}^{+0.07}$	$3.8_{-0.2}^{+0.1}$	$-1.73_{-0.38}^{+0.24}$	244_{-3}^{+3}	$29.9_{-1.2}^{+1.3}$
J0938+5428	0.102247	11_{-2}^{+1}	$20.63_{-0.11}^{+0.05}$	$4.3_{-0.2}^{+0.1}$	$-2.44_{-0.56}^{+0.45}$	291_{-4}^{+5}	$31.8_{-1.7}^{+3.9}$
J0942+3547	0.015010	69_{-0}^{+0}	$18.58_{-0.03}^{+0.03}$	$3.3_{-0.0}^{+0.0}$	$-3.67_{-0.73}^{+0.58}$	170_{-1}^{+1}	$18.4_{-0.2}^{+0.2}$
J0944-0038	0.004912	70_{-3}^{+3}	$19.42_{-0.08}^{+0.06}$	$3.9_{-0.2}^{+0.3}$	$-2.21_{-0.71}^{+0.54}$	217_{-4}^{+3}	$302.0_{-24.3}^{+23.0}$
J0944+3442	0.020138	59_{-10}^{+9}	$19.61_{-0.10}^{+0.11}$	$3.3_{-0.4}^{+0.9}$	$0.34_{-0.35}^{+0.23}$	179_{-11}^{+11}	$55.8_{-18.1}^{+18.3}$
J1016+3754	0.004024	81_{-2}^{+2}	$19.04_{-0.11}^{+0.13}$	$3.8_{-0.1}^{+0.3}$	$-0.58_{-0.08}^{+0.09}$	148_{-1}^{+2}	$21.6_{-1.3}^{+2.4}$
J1024+0524	0.033304	139_{-3}^{+3}	$19.05_{-0.11}^{+0.12}$	$4.6_{-0.1}^{+0.1}$	$-0.69_{-0.08}^{+0.14}$	192_{-2}^{+2}	$20.0_{-0.8}^{+2.5}$
J1025+3622	0.126552	131_{-4}^{+2}	$19.43_{-0.08}^{+0.07}$	$3.9_{-0.2}^{+0.3}$	$-1.31_{-0.35}^{+0.34}$	243_{-3}^{+3}	$38.2_{-2.3}^{+3.6}$
J1044+0353	0.012998	158_{-9}^{+9}	$18.40_{-0.13}^{+0.11}$	$3.4_{-0.3}^{+0.3}$	$-1.16_{-0.63}^{+0.44}$	253_{-8}^{+12}	$9.9_{-0.8}^{+0.9}$
J1112+5503	0.131497	153_{-4}^{+3}	$19.83_{-0.09}^{+0.06}$	$3.8_{-0.2}^{+0.2}$	$0.25_{-0.07}^{+0.08}$	257_{-4}^{+4}	$26.8_{-2.4}^{+2.7}$
J1119+5130	0.004532	1_{-2}^{+1}	$20.18_{-0.12}^{+0.10}$	$4.6_{-0.2}^{+0.1}$	$-0.91_{-0.26}^{+0.31}$	225_{-9}^{+9}	$13.2_{-4.6}^{+6.2}$
J1144+4012	0.126862	111_{-7}^{+12}	$20.19_{-0.07}^{+0.08}$	$4.8_{-1.0}^{+0.3}$	$0.48_{-0.19}^{+0.13}$	252_{-10}^{+8}	$324.8_{-63.3}^{+52.3}$
J1148+2546	0.045233	187_{-5}^{+6}	$19.66_{-0.11}^{+0.15}$	$5.0_{-0.2}^{+0.1}$	$-1.50_{-0.60}^{+0.58}$	265_{-8}^{+7}	$28.3_{-2.5}^{+4.7}$
J1157+3220	0.011074	392_{-2}^{+2}	$19.46_{-0.11}^{+0.12}$	$5.0_{-0.2}^{+0.1}$	$0.56_{-0.02}^{+0.03}$	118_{-1}^{+1}	$33.6_{-0.7}^{+4.8}$
J1200+1343	0.066828	131_{-3}^{+3}	$19.23_{-0.08}^{+0.17}$	$4.5_{-0.1}^{+0.2}$	$-0.04_{-0.04}^{+0.04}$	219_{-1}^{+1}	$86.3_{-3.1}^{+4.6}$
J1253-0312	0.022846	131_{-1}^{+1}	$19.28_{-0.04}^{+0.02}$	$4.2_{-0.1}^{+0.1}$	$-3.19_{-0.69}^{+0.70}$	246_{-1}^{+1}	$30.2_{-0.4}^{+0.4}$
J1323-0132	0.022511	26_{-1}^{+1}	$18.22_{-0.08}^{+0.06}$	$3.2_{-0.1}^{+0.0}$	$-0.95_{-0.05}^{+0.04}$	112_{-1}^{+1}	$87.5_{-1.2}^{+1.3}$
J1359+5726	0.033938	175_{-3}^{+3}	$19.30_{-0.08}^{+0.13}$	$4.6_{-0.2}^{+0.1}$	$-0.82_{-0.18}^{+0.23}$	125_{-2}^{+2}	$55.7_{-2.9}^{+3.5}$
J1416+1223	0.123174	-5_{-4}^{+4}	$19.20_{-0.08}^{+0.08}$	$3.6_{-0.3}^{+0.6}$	$0.38_{-0.10}^{+0.10}$	306_{-8}^{+7}	$41.7_{-2.6}^{+2.9}$
J1418+2102	0.008699	21_{-1}^{+1}	$19.73_{-0.02}^{+0.05}$	$4.1_{-0.1}^{+0.1}$	$-3.38_{-0.76}^{+0.58}$	246_{-1}^{+1}	$67.4_{-2.9}^{+2.9}$
J1428+1653	0.181544	122_{-3}^{+2}	$19.23_{-0.09}^{+0.05}$	$3.0_{-0.1}^{+0.2}$	$0.21_{-0.08}^{+0.07}$	168_{-3}^{+2}	$46.5_{-3.4}^{+3.3}$
J1429+0643	0.173649	21_{-2}^{+2}	$19.95_{-0.04}^{+0.09}$	$3.4_{-0.1}^{+0.2}$	$-1.30_{-0.05}^{+0.06}$	321_{-6}^{+5}	$41.6_{-2.1}^{+2.1}$
J1521+0759	0.094335	141_{-4}^{+3}	$19.40_{-0.08}^{+0.08}$	$5.0_{-0.1}^{+0.1}$	$-1.21_{-0.23}^{+0.22}$	97_{-4}^{+4}	$9.5_{-0.7}^{+1.1}$
J1525+0757	0.075916	133_{-2}^{+1}	$18.58_{-0.07}^{+0.09}$	$4.7_{-0.2}^{+0.1}$	$-1.09_{-0.11}^{+0.12}$	44_{-2}^{+2}	$20.1_{-1.0}^{+1.0}$
J1545+0858	0.037834	92_{-2}^{+2}	$19.43_{-0.06}^{+0.06}$	$4.2_{-0.2}^{+0.1}$	$-1.87_{-0.40}^{+0.34}$	72_{-2}^{+3}	$37.0_{-1.1}^{+1.8}$
J1612+0817	0.149198	187_{-2}^{+4}	$19.79_{-0.07}^{+0.08}$	$5.0_{-0.2}^{+0.2}$	$0.42_{-0.02}^{+0.03}$	84_{-2}^{+2}	$94.9_{-4.8}^{+5.1}$

Note. (1) Object name; (2) redshift estimated by the shell model; (3) outflow velocity of expanding shell; (4) HI column density; (5) temperature; (6) dust extinction; (7) intrinsic line width; (8) equivalent width.

(This table is available in machine-readable form.)

DLA system at $N_{\text{HI}} \approx 10^{21} \text{ cm}^{-2}$. We recognize that the DLA sightlines and the pathways of the scattered Ly α emission select specific channels through a turbulent, multiphase ISM. Nonetheless, their combined distribution may represent a large fraction of all sightlines because we found that these components cover complementary fractions of the UV continuum (see Sections 2 and 3).

We weight the column densities by the covering fraction of each system in the middle panel of Figure 11. This normalization indicates how many sightlines are covered by the low- N_{HI} or high- N_{HI} paths. After accounting for the covering fraction, the peak of the distribution of low- N_{HI} paths shifts to a lower-column density; the lower-column densities have higher weights, i.e., larger covering fraction of low- N_{HI} paths. In other words, the galaxies with only Ly α emission line observed have lower-column densities compared to those showing Ly α emission in the bottom of DLA system.

In the bottom panel, we present the combined distribution of column densities in galaxies with only Ly α emission, only DLA system, or Ly α emission in the bottom of DLA system. Similar to the middle panel, the distributions are weighted by the covering fraction. Clearly, the column densities increase

with the presence of DLA system, consistent with the middle panel. Overall, however, the distribution remains bimodal, consistent with the argument that the distribution includes a large fraction of all sightlines. At a qualitative level, the bimodal distributions in Figure 11 confirm a structural similarity between the ISM in CLASSY galaxies and the ISM in hydrodynamical simulations focusing on the star—gas interplay (Ma et al. 2020; Kakiichi & Gronke 2021). In detail, however, we recognize several quantitative differences.

4.1.2. Column Density Distribution in Simulations

In the H II region simulations of Kakiichi & Gronke (2021), turbulence driven by ionization fronts creates a bimodal distribution of column densities. In their Figure 6, the higher-column-density peak covers N_{HI} values similar to our Figure 11. The simulated column density distribution actually reaches a minimum around 10^{19} cm^{-2} , however, right where Figure 11 shows a maximum. The lower-column-density peak is offset to 10^{17} cm^{-2} in the simulated distribution. These simulations zoom in on the individual H II region, and it is

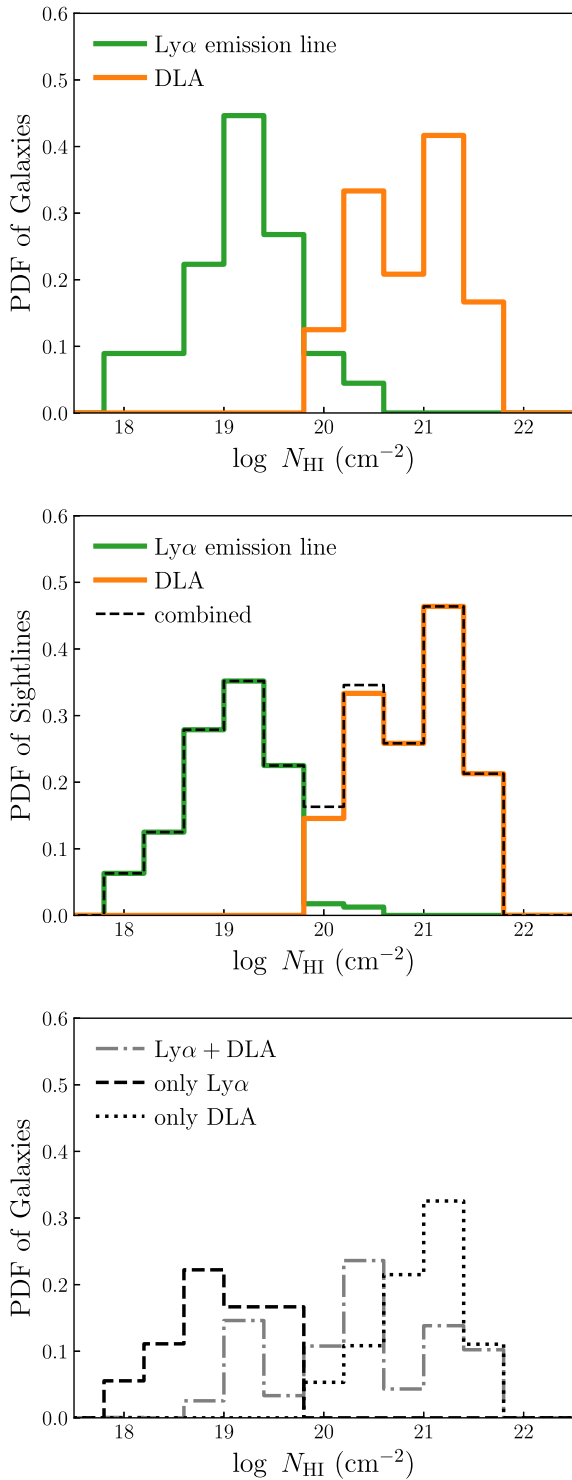


Figure 11. The probability distribution functions of column densities derived by the DLA fitting (orange line) and the Ly α profile fitting (green line). In the top panel, the histograms are normalized by the total numbers of galaxies showing DLA system (31) or Ly α emission line (28 after excluding the J0808 +3948 active galactic nucleus), respectively. In the middle panel, the histogram is weighted by the covering fraction of low- N_{HI} and high- N_{HI} paths: $(1 - f_c)$ and f_c , respectively. The black dashed line represents the combined distribution over the $\sim 10^{18}$ – 10^{22} cm^{-2} range for CLASSY galaxies. In the bottom panel, we present the distribution of column densities for three types of Ly α profiles. The black dashed line indicates the galaxies with only Ly α emission, the gray dashed-dotted line indicates the galaxies with Ly α emission in the bottom of DLA system, and the dotted line indicates the galaxies with only DLA systems. The resulting distribution remains bimodal regardless of the details of the weighting and subsample.

possible that placing the H II region in a more realistic galactic environment would shift the distribution.

Comparing the histogram in Figure 11 to those from Figure 11 of Ma et al. (2020), we find the high- N_{HI} gas spread over a similar range in column density. In those simulations, the fraction of high- N_{HI} is sensitive to galaxy mass; for their 10^7 – $10^8 M_{\odot}$ sample, the fraction of sightlines with high- N_{HI} to the total H I sightlines is about one-third as large seen in Figure 11. Since their histograms exclude the gas within $0.2R_{\text{vir}}$ of the starburst, it is possible that the addition of the starburst region would eliminate, or at least mitigate, the discrepancy. Another difference is the column density of the lower-density peak. This peak is seen at $N \approx 18$ – 20 cm^{-2} in CLASSY, whereas Ma et al. (2020) find the low- N_{HI} channels spread, primarily, over the $N \approx 16$ – 18 cm^{-2} range. This result may indicate that the feedback in Ma et al. (2020) is too efficient and removes too much neutral hydrogen.

Integral-field spectroscopy is clearly needed to address two observational biases. The histograms in Figure 11 combine measurements made on different physical scales because the physical size of the aperture changes with galaxy distance. It is not fully understood how the aperture affects the column density derived by shell-model fitting. In addition, we emphasize that the lowest-column density sightlines may be missing from Figure 11. The shell model returns a column density that represents the total column of clouds plus an intercloud medium (Li & Gronke 2022); it follows that the lowest- (and highest-) column density sightlines may not be represented in Figure 11. The low- N_{HI} channels may therefore include lower-column-density pathways, and we aim to understand whether CLASSY galaxies have sightlines optically thin to LyC radiation.

4.2. Pathways for LyC Leakage

In this section, we will investigate the LyC-thin sightlines²⁴ with $N_{\text{HI}} < 10^{18} \text{ cm}^{-2}$ in CLASSY sample by analyzing the positive residual Ly α trough fluxes and small $\Delta v_{\text{Ly}\alpha}$.

4.2.1. Peak Separation, Trough Flux, and Red Asymmetry

Peak separation is a good, empirical tracer of LyC escape (Izotov et al. 2020), and the shell model provides a theoretical basis for this relation (Dijkstra et al. 2016; Eide et al. 2018). In galaxies where there are few holes through which LyC can escape (low LyC leakage), the scattered Ly α photons traverse optically thick channels, leading to a broad peak separation. Whereas, in galaxies with high LyC leakage, the density-bounded channels result in a small peak separation. However, the peak separation does not distinguish how the Ly α photons escape (Kakiichi & Gronke 2021), as many small holes in a turbulent medium can produce a narrow peak separation just like a large, wind-blown cavity.

The Ly α asymmetry parameter A_f helps to quantify the multiphase nature of the turbulent H II regions. It is originally introduced by Rhoads et al. (2003) to measure the attenuation imprinted by IGM at high-redshift. Here, we apply it in a different context recently introduced by Kakiichi & Gronke (2021). The two dominant types of Ly α escape (single flight or excursion) tend to produce a symmetric Ly α line. Thus, when the medium is dominated either by ionization- or density-

²⁴ Column densities lower than 10^{18} cm^{-2} correspond to LyC escape fractions $\gtrsim 1\%$ (Kakiichi & Gronke 2021).

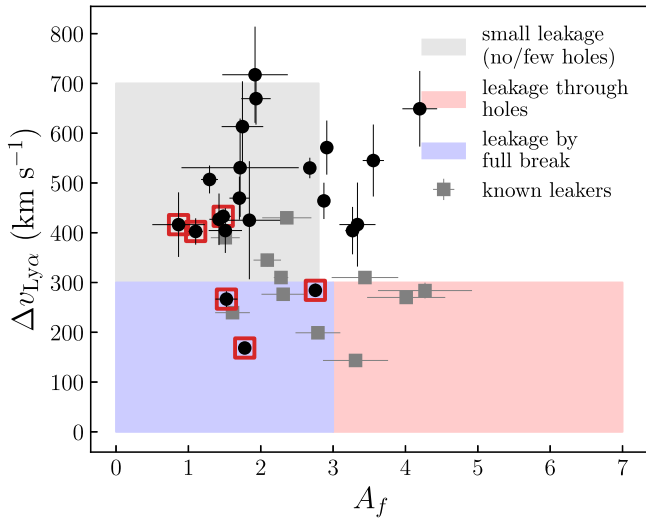


Figure 12. Ly α red peak asymmetry vs. Ly α peak separation. The gray, blue, and pink shaded regions correspond to three different regimes of LyC leakage: small leakage (gray), leakage through low- N_{HI} holes (small holes, red), and leakage by the full break (large density-bounded holes, blue), respectively. We overplot the known leakers from Izotov et al. (2016, 2018a, 2018b) as gray squares. The red squares highlight six galaxies (J0942+3547, J0944-0038, J1253-0312, J1323-0132, J1418+2102, J1545+0858), which have net Ly α trough flux, suggesting they might be LyC leakers.

bounded channels as in the blue or gray region in Figure 12, the asymmetry of the emergent line is low. However, when the two channels coexist as in the red region in Figure 12, the asymmetry is high.

In Figure 12, we plot Ly α peak separation against red peak asymmetry. We divide the diagram into three distinct regions: (gray) low LyC leakage, (red) significant leakage through low- N_{HI} channels (ionization-bounded, $f_{\text{esc}}^{\text{LyC}} > 10\%$), and (blue) significant through large holes (density-bounded, $f_{\text{esc}}^{\text{LyC}} > 10\%$). The boundaries come from Figure 13 of Kakiichi & Gronke (2021), which shows these regions in the $\Delta v_{\text{Ly}\alpha}$ - $f_{\text{esc}}^{\text{LyC}}$ and A_f - $f_{\text{esc}}^{\text{LyC}}$ planes. We find that the strongest LyC leakers in CLASSY are the three galaxies—J0942+3547, J1323-0312, J1545+0858—in the blue region.

The Ly α profiles of these three galaxies also show residual fluxes at Ly α trough: $F_{\text{trough}}/F_{\text{cont}} = 1.36 \pm 0.07$, 19.62 ± 0.42 , 0.17 ± 0.12 , respectively. Their net Ly α trough flux supports the conclusion that these galaxies have LyC-thin sightlines (Verhamme et al. 2015; Gazagnes et al. 2020). Based solely on their Ly α profile properties then, these galaxies are likely strong LyC leakers. When we compare their location in Figure 12 to directly confirmed LyC leakers, we find that their peak separation is as small as the smallest values measured among directly confirmed LyC leakers (Izotov et al. 2016, 2018a, 2018b).

Many CLASSY galaxies are located in the gray-shaded region of Figure 12, suggesting they have lower LyC escape fractions than the three galaxies in the blue zone. Three known leakers from Izotov et al. (2016, 2018a, 2018b) also lie in the gray zone of Figure 12, just 100 km s^{-1} above the blue-gray boundary. Based on this comparison to the Ly α properties of the known leakers, we suggest that the CLASSY sample contains more LyC leakers than the (blue) shaded region indicates. The Kakiichi & Gronke (2021) simulations zoom in on individual H II regions, so perhaps, the boundary might shift 100 km s^{-1} in more realistic environments, i.e., those composed of multiple H II regions.

To gain insight into the empirical boundary, we inspect the positions of the other three CLASSY galaxies with net Ly α trough flux. Nonzero trough flux in the emission-line profile requires a low- N_{HI} column at the systemic velocity. We find three more galaxies with net trough flux, and each has $\Delta v_{\text{Ly}\alpha} < 400 \text{ km s}^{-1}$. The galaxies are J0944-0038, J1253-0312, and J1418+2102; their trough fluxes are $F_{\text{trough}}/F_{\text{cont}} = 0.47 \pm 0.29$, 0.22 ± 0.07 , 1.46 ± 0.17 , respectively.

We acknowledge that Ly α trough fluxes are sensitive to the spectral resolution, which is not precisely known for the Ly α emission. We therefore compared the Ly α trough width to the width of the red peak, which represents an upper limit on the unresolved linewidth. Four galaxies (0942+3547, J1323-0312, J1545+0858, J1418+2102) show broader Ly α trough widths than the Ly α peak widths, so these troughs are clearly resolved. For the other two objects, J0944-0038 and J1253-0312, their Ly α trough widths are similar to Ly α peak widths, so higher-resolution spectroscopy might find that we possibly overestimate their residual trough flux. Consequently, we identified at least four CLASSY galaxies containing density-bounded channels.

We conclude that the empirical boundary between the blue and gray zones lies closer to a peak separation of 400 km s^{-1} , roughly 100 km s^{-1} larger than the blue-gray boundary suggested by the simulations. Based solely on the properties of Ly α line profiles, we conclude that four to six of the CLASSY galaxies (highlighted by red squares in Figure 12) are strong LyC leakers. Their red peaks have a low asymmetry, $A_f < 3$, which indicates they are best described as density-bounded galaxies. In contrast, even though they span the same range of peak separations, half of the directly confirmed leakers have $A_f > 3$, suggesting their leakage is through ionization-bounded channels in a multiphase medium.

4.2.2. Combining Perspectives from Ly α and O32

In the previous section, we have shown that the Ly α trough flux, Ly α peak separation, and Ly α red peak asymmetry converge at the same selection of galaxies with density-bounded holes in their neutral ISM. Here, we examine the ionization structure of these galaxies, as measured by optical nebular emission lines, to reveal the underlying relation between LyC leaking channels and ionization. We adopt [O III] $\lambda 5007$ /[O II] $\lambda 3727$ (O32) ratio, one of the most important ionization diagnostics (Kewley et al. 2019), where a high O32 ratio can indicate a density-bounded galaxy²⁵ (Jaskot & Oey 2013; Nakajima & Ouchi 2014; Izotov et al. 2016; Flury et al. 2022).

$f_{\text{esc}}^{\text{Ly}\alpha}$ and O32. Intuitively, we expect a high escape fraction of Ly α photons from density-bounded galaxies. Yet, in the top panel of Figure 13, the O32 ratio shows no correlation with $f_{\text{esc}}^{\text{Ly}\alpha}$ (Spearman coefficient ~ 0.04), contradicting the correlation observed among high-redshift galaxies (Trainor et al. 2019) and among local dwarf galaxies (Hayes et al. 2023). We argue here that the lack of correlation in our sample might result from the scattering of Ly α photons outside the COS aperture, an effect that we argued produces DLA systems in many CLASSY spectra (see Section 2.2).

²⁵ Two of our three best candidates for density-bounded galaxies, J1323-0312 and J1545+0858, have the largest O32 ratios among the CLASSY sample (37.8 and 8.6, respectively). On the other hand, J0942+3547 has a lower O32 ratio of 2.6.

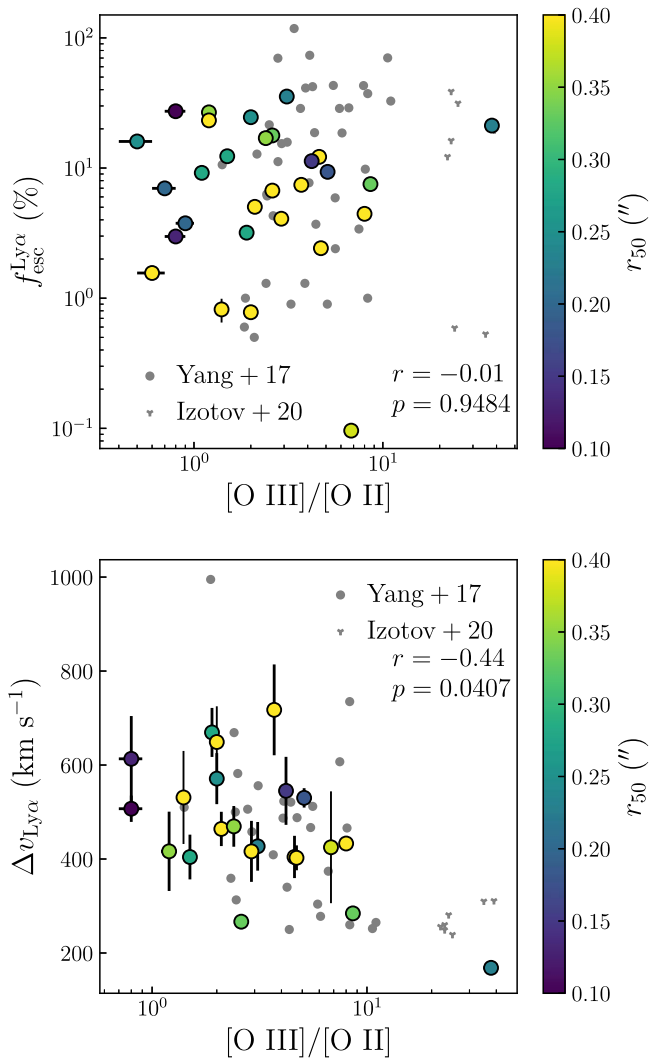


Figure 13. $f_{\text{esc}}^{\text{Ly}\alpha}$ (top) and $\Delta v_{\text{Ly}\alpha}$ (bottom) vs. O32 ratio. The O32 ratio is defined as $[\text{O III}] \lambda 5007 / [\text{O II}] \lambda 3727$. We color-code the circles based on their UV half-light radius. The yellow circles have a UV half-light radius larger than $0''.4$, which corresponds to the COS unvignetting aperture. We overplot the data in the literature to expand the dynamic range. The gray dots indicate the dwarf galaxies at $z \sim 0.1\text{--}0.4$ from Yang et al. (2017). The gray Y-shape markers indicate the local dwarf galaxies at $z \sim 0.02\text{--}0.07$ with extreme O32 ratios from Izotov et al. (2020).

The slits used to observe high-redshift galaxies in Trainor et al. (2019) typically subtend 5 to 10 kpc, much larger than the physical scale subtended by the COS aperture for the lowest-redshift targets. Although the *Lyman Alpha Spectral Database* (LASD; Runnholm et al. 2021; Hayes et al. 2023) includes some low-redshift galaxies, the CLASSY sample has a lower median redshift than LASD, so scattering outside the COS aperture plausibly introduces a more serious bias. To test this explanation, we restrict the analysis to the subsample with UV radius $< 0''.4$, the radius of the unvignetted COS aperture, and find a positive correlation; among the yellow points in Figure 13, the Spearman coefficient of 0.22.

However, the galaxy distance might not be the only factor influencing scattering outside the spectroscopic aperture. The Ly α escape fraction of higher-redshift galaxies may also be significantly affected. In the top panel of Figure 13, we overplot measurements for Green Pea galaxies at redshift 0.1–0.4 (Yang et al. 2017). We add LyC leakers from

Izotov et al. (2020) with extreme O32 ratios (ranging from 22 to 39). Although the joint sample has a similar redshift range as Hayes et al. (2013), it also shows no correlation between $f_{\text{esc}}^{\text{Ly}\alpha}$ and O32 ratio. A subset of the joint targets with a large O32 ratio has modest $f_{\text{esc}}^{\text{Ly}\alpha}$ of $\sim 1\%$. Thus, using $f_{\text{esc}}^{\text{Ly}\alpha}$ to probe the density-bounded channels should always be aware of those exceptions, not only the aperture loss.

$\Delta v_{\text{Ly}\alpha}$ and O32. Consistent with previous studies (Yang et al. 2017; Jaskot et al. 2019; Izotov et al. 2020; Hayes et al. 2023), the Ly α peak separation $\Delta v_{\text{Ly}\alpha}$ among CLASSY galaxies is anticorrelated with the O32 ratio, as shown in the bottom panel of Figure 13. Excluding the galaxies with large UV radius ($> 0''.4$) does not change the correlation strength, and thus, we conclude that the Ly α peak velocity measurements are only weakly affected by the aperture loss. The Ly α profiles of LyC leakers with extreme O32 ratios of 22–39 from Izotov et al. (2020) show $\Delta v_{\text{Ly}\alpha} \approx 250 \text{ km s}^{-1}$, similar to the J1545+0858 and J0942+3547 in CLASSY sample, consistent with a minimum $\Delta v_{\text{Ly}\alpha}$ around 250 km s^{-1} . The only data in Figure 13 with lower $\Delta v_{\text{Ly}\alpha}$ our new data point for J1323-0312.

The joint sample shows that high O32 galaxies always have narrow peak separations, while the low O32 galaxies spread a large range of $\Delta v_{\text{Ly}\alpha}$. We argue that a high O32 ratio traces a large global covering fraction of LyC-thin sightlines, whereas the narrow Ly α peak separations appear when the covering fraction of LyC-thin sightlines in our direction is high. The variations in the direction of LyC-thin sightlines relative to our viewing angle, therefore, produce the scatter observed in the $\Delta v_{\text{Ly}\alpha}$ versus O32 ratio diagram.

The correlation between $\Delta v_{\text{Ly}\alpha}$ and O32, and the non-correlation between $f_{\text{esc}}^{\text{Ly}\alpha}$ and O32 might hint that the different Ly α features probe Ly α photons from different channels. This speculation is in line with the simulations of Kakiichi & Gronke (2021). When the pathways for LyC escape have a low covering fraction, the majority of Ly α photons still need to escape through low- $N_{\text{HI}} \approx 10^{18}\text{--}10^{20} \text{ cm}^{-2}$ channels, the Ly α emission line emerges with a broad width and large peak separation. Meanwhile, a smaller fraction of Ly α photons will pass through the remaining columns, which are optically thin to the LyC ($< 10^{18} \text{ cm}^{-2}$), and these sightlines contribute Ly α emission with narrow lines and small peak-separation (see Figure 12 in Kakiichi & Gronke 2021). It follows that the transition from ionization-bounded leakers to density-bounded leakers is accompanied by a change in the shape of the Ly α profiles (namely, the relative strength of the narrow and broad lines). As the covering fraction of LyC thin holes increases, more of the emergent Ly α flux is contributed by the component with narrow peaks. When the intensities of two narrow peaks are larger than those of broad peaks, these LyC thin channels can determine $\Delta v_{\text{Ly}\alpha}$ while the covering fraction of channels with $> 10^{18}$ remains significant and continues to produce broad peaks with a wider separation. Thus, in the case of a significant covering fraction of LyC-thin holes, the peak separation is probing the HI column in LyC-thin holes, and we expect O32 to increase as $\Delta v_{\text{Ly}\alpha}$ decreases. However, in the case of no LyC leakage or a small LyC leakage, the Ly α photons that pass through the columns $> 10^{18} \text{ cm}^{-2}$ dominate the Ly α profile (peaks and wings).

4.3. Outflow Velocity of Neutral ISM

Chevalier & Clegg (1985) described an adiabatic galactic wind that could reach speeds of roughly 1000 km s^{-1} .

Theoretical models that explain the relation of this hot phase to the widely observed cool outflows have been a subject of studies for an extended period of time (Klein et al. 1994; Schneider & Robertson 2018; Fielding & Bryan 2022). Photoionization modeling of the LIS absorption lines in CLASSY spectra indicates the outflowing component traces gas in which hydrogen is mostly ionized (Xu et al. 2022). Yet, the combined neutral and molecular phases transport as much (or more) mass than does the warm-ionized phase in the outflow from M82 (Martini et al. 2018; Yuan et al. 2023).

Since Ly α probes the portion of the outflow where hydrogen is neutral, the outflow detection using Ly α complements studies of the highly ionized outflow. When Ly α photons scatter in outflowing gas, the resonance center will move blueward with respect to the rest-frame Ly α line center. Consequently, the outflow velocity is imprinted on the Ly α profile. Here, we suggest that the $v_{\text{trough}}^{\text{Ly}\alpha}$ indicates the average outflow velocity v of neutral clouds, where $-v$ corresponds to the largest optical depth (Orlitova et al. 2018; Michel-Dansac et al. 2020; Li & Gronke 2022). In this section, we first compare Ly α trough velocity $v_{\text{trough}}^{\text{Ly}\alpha}$ against the Doppler shift of LIS lines. Then, we compare the outflow speeds of neutral ISM in low- $N_{\text{H I}}$ channels, Ly α trough velocity $v_{\text{trough}}^{\text{Ly}\alpha}$, to tracers of high- $N_{\text{H I}}$ clouds. Finally, adopting $v_{\text{trough}}^{\text{Ly}\alpha}$ as a direct measurement of the mean Doppler shift of the neutral gas, we revisit why radiative-transfer modeling is typically driven toward a shell velocity faster than $v_{\text{trough}}^{\text{Ly}\alpha}$.

4.3.1. Ly α Trough Velocity and LIS Velocity

Resonance UV absorption lines, e.g., Si II and C II, have been extensively used to measure outflow speeds (e.g., Henry et al. 2015; Reddy et al. 2016; Orlitova et al. 2018; Hayes et al. 2023). Here, we focus on Si II λ 1260, which is well measured by the CLASSY collaboration.

The Doppler shifts of Si II in the CLASSY sample have been measured using two different methods. Xu et al. (2022) use a double-Gaussian profile to deblend the outflow component from the static ISM component of Si II and find that the outflow component is mostly ionized. On the other hand, K. Parker et al. (2023, in preparation) fit a single-Voigt profile to determine the average velocity of all LIS absorbers. As the LIS lines can also arise from the neutral ISM, the Parker measurements should include the contribution of neutral ISM. Conceptually, if the LIS absorber is dominated by the static ISM, the Parker measurement, which is close to 0 km s $^{-1}$, should be distinct from the Xu measurement. But if the LIS absorber is dominated by the outflow component, the Parker measurement should be similar to the Xu measurement.

Figure 14 presents the comparisons of $v_{\text{trough}}^{\text{Ly}\alpha}$ to both LIS outflow measurements derived by the two methods.²⁶ Directly comparing the two LIS outflow measurements in the top and bottom panels, we notice the positions of two objects (J1416+1223, J0938+5428) shift significantly. K. Parker et al. (2023, in preparation) derive a velocity close to 0 km s $^{-1}$, but the outflow velocities derived in Xu et al. (2022) can reach several hundred kilometers per second, suggesting the LIS absorbers of these two galaxies are mainly static. The galaxies that shift between the two panels have substantial absorption at $v=0$, which we attribute to the static ISM.

²⁶ J0808+3948 is excluded because its polycyclic aromatic hydrocarbon feature suggests it might be an active galactic nucleus (Xie et al. 2014).

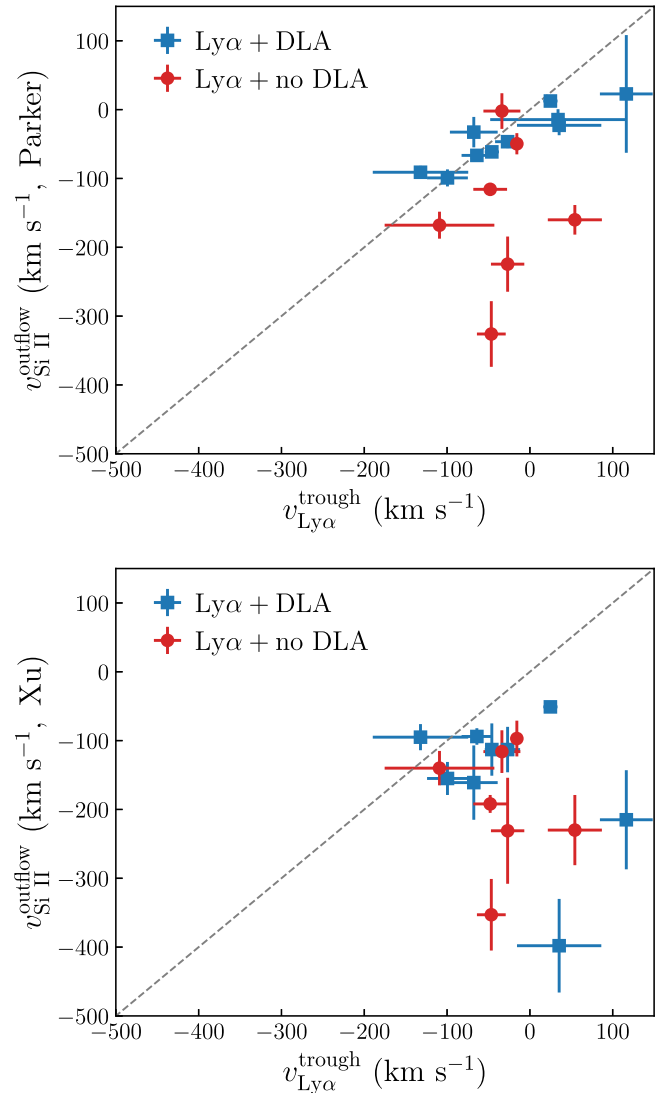


Figure 14. $v_{\text{Si II}}^{\text{outflow}}$ vs. $v_{\text{trough}}^{\text{Ly}\alpha}$. The top panel adopts the $v_{\text{Si II}}^{\text{outflow}}$ measured by the single-Voigt fitting (K. Parker et al. 2023, in preparation), and the bottom panel adopts the $v_{\text{Si II}}^{\text{outflow}}$ measured by a double-Gaussian fitting (Xu et al. 2022). The dashed lines indicate the 1:1 relationship. The Si II absorbers are multiphase, including neutral hydrogen in addition to the mostly ionized phase. By comparing $v_{\text{trough}}^{\text{Ly}\alpha}$ and $v_{\text{Si II}}^{\text{outflow}}$, we are able to distinguish ionization status of the ISM.

Second, we see that the Si II velocity measured by K. Parker et al. (2023, in preparation) shows a better agreement with $v_{\text{trough}}^{\text{Ly}\alpha}$, particularly the galaxies with both Ly α and DLAs (blue squares) in the top panel of Figure 14. This suggests that, in those galaxies, the Si II absorbers (in both outflow and static) contain a significant fraction of neutral hydrogen, although Xu et al. (2022) suggest that the Si II in the outflow traces mostly ionized gas.

However, looking at the galaxies with no DLAs (red circles in Figure 14), their Si II velocities disagree with $v_{\text{trough}}^{\text{Ly}\alpha}$ in both two panels. The three most deviant circles (J0021+0052, J0926+4427, J1429+0643) show that their $v_{\text{trough}}^{\text{Ly}\alpha}$ are close to 0 km s $^{-1}$, but the Si II velocities are ≤ -200 km s $^{-1}$. We find that their Si II line profiles are dominated by the outflow component: they have very little absorption at the systemic velocity, so the velocity is not sensitive to the measurement method. This suggests that the Si II absorption comes mostly

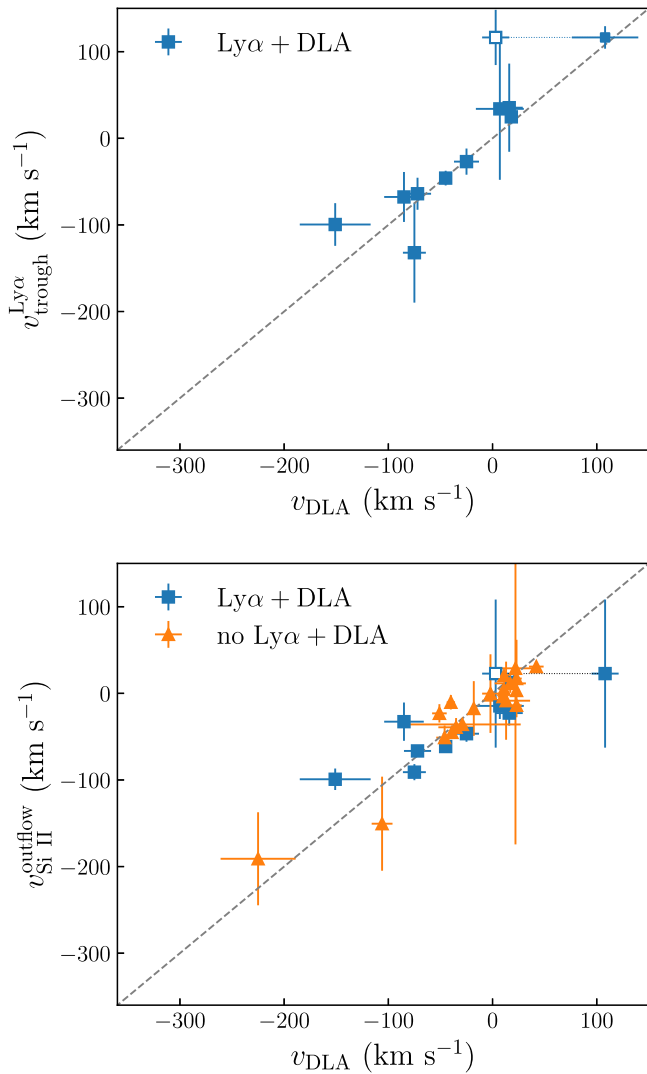


Figure 15. v_{DLA} vs. $v_{\text{trough}}^{\text{Ly}\alpha}$ (top) and $v_{\text{Si II}}^{\text{outflow}}$ (bottom). Here, we adopt the $v_{\text{Si II}}^{\text{outflow}}$ measured by K. Parker et al. (2023, in preparation). The gray dashed lines indicate the 1:1 relationship. In the bottom panel, we separate the sample based on whether their spectra have $\text{Ly}\alpha$ emission lines. We notice the O I absorption line of one galaxy (J0938+5428, open square) is contaminated by the refilling O I emission line. Thus, we adopt the velocity of C II absorption line, and we use a black dashed line to connect them. The good agreement suggests that the gas in low- $N_{\text{H I}}$ has same velocity as the gas in high- $N_{\text{H I}}$ channels.

from the ionized gas in these galaxies, similar to Xu et al. (2022).

4.3.2. $\text{Ly}\alpha$ Trough Velocity and DLA Velocity

In the top panel of Figure 15, we compare the $\text{Ly}\alpha$ trough velocity $v_{\text{trough}}^{\text{Ly}\alpha}$ and the velocity of high- $N_{\text{H I}}$ clouds (i.e., DLA system velocity probed by O I absorption line). It is intriguing to see such a good agreement between these two independent measurements, suggesting that the low- $N_{\text{H I}}$ channels have the same velocity as the high- $N_{\text{H I}}$ channels.

In the bottom panel of Figure 15, we further find that DLA velocity agrees with Si II velocity. Here, we include the galaxies, which do not have $\text{Ly}\alpha$ emission lines, as the circles. They are consistent with those galaxies that have both $\text{Ly}\alpha$ emission lines and DLA systems. This hints that, for the galaxies with DLA systems, the intrinsic reason for the

correlation between Si II velocity and $v_{\text{trough}}^{\text{Ly}\alpha}$ is that the Si II mainly traces the high- $N_{\text{H I}}$ clouds, and the high- $N_{\text{H I}}$ clouds have similar velocity as the low- $N_{\text{H I}}$ clouds.

4.3.3. Revisiting Outflow Velocity Discrepancy

In this section, we discuss the outflow velocity discrepancy using the same profile fittings as Section 3.3 and propose a new explanation of the discrepancies. Here, we adopt the $v_{\text{trough}}^{\text{Ly}\alpha}$ as the intrinsic outflow velocity since it traces the neutral ISM, which scatters the $\text{Ly}\alpha$ photons.

First, we directly compare the $v_{\text{trough}}^{\text{Ly}\alpha}$ measured based on the spectroscopic redshift and the outflow velocities v_{tlac} estimated by the shell model. In the top panel of Figure 16, we present the comparison for both the second profile fitting (redshift-unconstrained) and the third profile fitting (redshift-constrained). Although a clear correlation between $v_{\text{trough}}^{\text{Ly}\alpha}$ and v_{tlac} can be seen, v_{tlac} is larger by 0–200 and 0–140 km s^{-1} than the $v_{\text{trough}}^{\text{Ly}\alpha}$ for the second and third fittings, respectively.

We speculate that the reason for this discrepancy is a redshift error required by the model fitting. To test this idea, we shift our $v_{\text{trough}}^{\text{Ly}\alpha}$ measurements to the fictitious reference frame chosen by the fitted tlac redshift.

The bottom panel of Figure 16 shows the $v_{\text{trough}}^{\text{Ly}\alpha}$ measurements in the tlac reference frames defined by the second and third fittings. We have shifted the measurements by

$$v_{\text{trough}, z_{\text{tlac}}}^{\text{Ly}\alpha} = v_{\text{trough}}^{\text{Ly}\alpha} - (z_{\text{tlac}} - z_{\text{spec}}) \times c, \quad (5)$$

where c is the speed of light. The new correlations are significantly improved and close to the 1:1 relationship. In particular, for the redshift-unconstrained fitting (second attempt), $v_{\text{trough}}^{\text{Ly}\alpha}$ and v_{tlac} agree well with each other. These results confirm that we should compare $v_{\text{trough}}^{\text{Ly}\alpha}$ and v_{tlac} in a common redshift frame. This also confirms that the outflow velocity and the redshift are coupled in the shell model:

$$\frac{\lambda_{\text{trough}}^{\text{Ly}\alpha}}{(1+z) \times \lambda_{\text{Ly}\alpha}} - 1 = -\frac{v_{\text{outflow}}}{c}, \quad (6)$$

where $\lambda_{\text{trough}}^{\text{Ly}\alpha}$ is the wavelength of $\text{Ly}\alpha$ trough, and $\lambda_{\text{Ly}\alpha}$ is the rest-frame wavelength of $\text{Ly}\alpha$. Once the redshift of the shell model is fixed, the model outflow velocity is also determined by the Doppler offset of the observed $\text{Ly}\alpha$ trough with respect to the model redshift. Thus, the redshift and outflow velocity discrepancies are the *two sides of the same coin*.

The preferred larger outflow velocity by tlac may hint that the observed B/R ratio is lower than the intrinsic B/R ratio. Moreover, as we discussed in Section 2.2, the observed B/R ratio can be biased by the aperture loss. Thus, this inspires us to connect the discrepancies to the aperture loss.

We, therefore, propose an explanation for the discrepancies. Since the aperture loss modifies the B/R ratio to a lower value and the B/R ratio is tightly anticorrelated with outflow velocity, to achieve the smaller observed B/R ratio, the shell model will suggest a larger outflow velocity. Meanwhile, a higher systematic redshift is required to match the $\text{Ly}\alpha$ trough velocity to the outflow velocity (Equation (6)). Thus, the best-fit redshift and outflow velocity from the shell model are larger than that observed from the spectra. The aperture loss has a nonnegligible impact on the $\text{Ly}\alpha$ profile and should always be considered when interpreting $\text{Ly}\alpha$ profile.

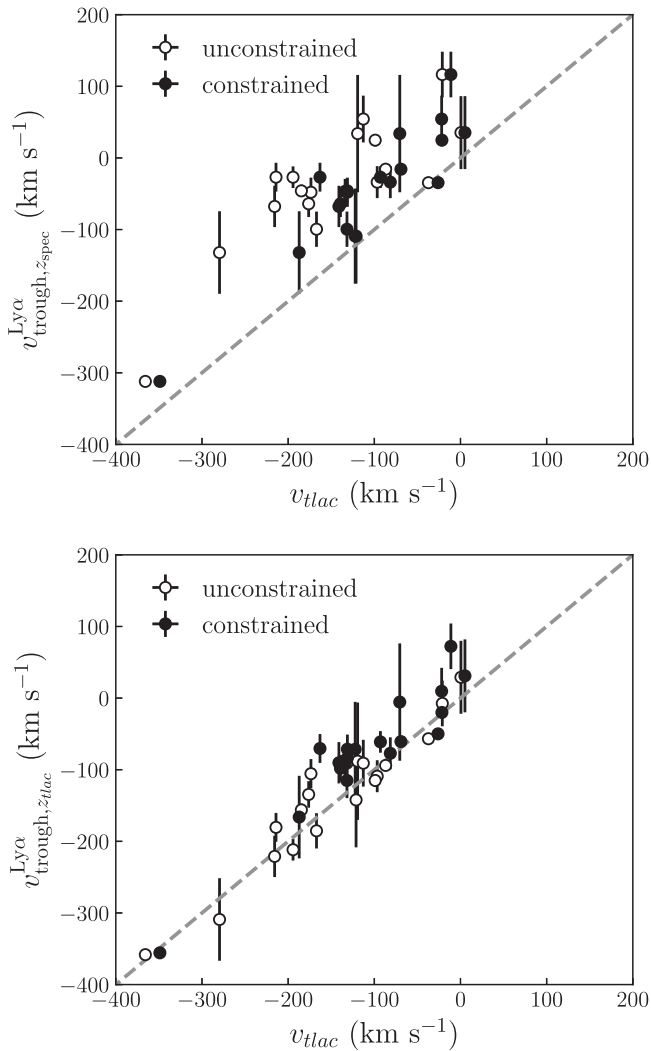


Figure 16. The Ly α trough velocity measured from spectrum vs. the outflow velocity estimated by the shell model. Top panel: the $v_{\text{trough}}^{\text{Ly}\alpha}$ is measured based on the spectroscopic redshift. Bottom panel: the $v_{\text{trough}}^{\text{Ly}\alpha}$ is measured based on the redshift from tlac profile fitting. We plot the measurements from both the z -unconstrained fitting (open circle, Section 3.2.2) and the z -constrained fitting (solid circle, Section 3.3). The dashed line indicates the 1:1 relationship.

4.4. A Schema of the Neutral ISM

In this section, we summarize our interpretation of ISM structure from the previous sections. We have demonstrated that the ISM in CLASSY galaxies is inhomogeneous, consisting of high- N_{HI} , low- N_{HI} , and even LyC-thin regions, based on the clear separation between the DLA and Ly α emission (see Section 3.2), the nonzero residual flux at Ly α trough, and small peak separation (see Section 4.1). In the left panel of Figure 17, we plot a schema of the neutral ISM for illustration. For simplicity, we adopt a continuous shell model. The low- N_{HI} and high- N_{HI} paths are shown as light blue and dark blue, respectively. We also use two gray shades to indicate the Ly α halos missed due to the aperture effect. In the right panel, we zoom in to show the Ly α radiative transfer in a small slab. The green lines indicate the Ly α photons, and the gray lines indicate the continuum photons.

Although the Ly α radiative process is highly nonlinear and nonadditive, the radiative transfer fitting results suggest that we can take the Ly α emission and DLA system apart. The DLA

system can be well fitted by a partial-covering Voigt profile with a high- N_{HI} , and the Ly α emission normalized by the uncovered continuum can be well fitted by the shell model with a low- N_{HI} . This clear separation between Ly α emission and DLA system indicates that the Ly α exchange between low- N_{HI} path and high- N_{HI} path should be negligible, as we discussed in Section 3.2. Only very few Ly α photons that are injected into one region can travel to another region, and thus, the Ly α radiative processes in two different regions are independent. This is feasible because of two reasons: (1) the possibility of a Ly α photon traveling from low- N_{HI} path to high- N_{HI} path is very small, as most of which are just “reflected” by the surface between two channels (Hansen & Oh 2006); (2) the Ly α photons including the underlying continuum photons that are injected into high- N_{HI} paths are mostly scattered to much larger impact parameters (i.e., the extended Ly α halo, Steidel et al. 2011; Zheng et al. 2011); thus, most of which are missed due to the aperture effect and leave a DLA system. Thus, only the Ly α photons that escape through low- N_{HI} regions can be observed, and the emergent Ly α profile is a combination of Ly α spectra from two regions, as illustrated by the green and gray lines in Figure 17, and has a profile of Ly α emission in the bottom of DLA system.

In the left panel of Figure 17, we plot several low- N_{HI} channels in different directions. Although all of those low- N_{HI} channels can allow the escape of Ly α photons, only the channels exposed to the COS aperture (i.e., horizontal one in Figure 17) can contribute to the observed Ly α emission line. Because, for the Ly α photons that are initially injected into low- N_{HI} channels in other directions, they still need to penetrate the high- N_{HI} paths before reaching us.

We have proposed a scenario that the aperture loss is responsible for those unexpected profiles of Ly α emission in the bottom of DLA system in the CLASSY sample. In this work, we also find that the DLA absorber (neutral gas in high- N_{HI} paths) has a similar systematic velocity as the neutral gas in the low- N_{HI} paths. However, the ionized gas, traced by the outflowing component of Si II absorption line, has a generally larger velocity compared with that of the neutral gas in the low- N_{HI} paths.

Using three LyC leakage diagnostics, we find that at least three galaxies in the CLASSY sample are LyC leaker candidates. Thus, in the right panel of Figure 17, we use yellow to indicate the possible LyC-thin channels in the ISM, through which the Ly α photons can easily escape without much resonant scattering. By comparing the $\Delta v_{\text{Ly}\alpha}$ with O32 ratio, we conclude that the O32 ratio is tracing the covering fraction of LyC-thin channels, consistent with those known LyC leakers (Flury et al. 2022). The covering fraction increases as the O32 ratio increases, and thus, the probability of observing small $\Delta v_{\text{Ly}\alpha}$ increases.

5. Summary and Conclusions

In this paper, we extracted high-resolution Ly α line profiles from CLASSY spectra of 45 EoR analogs. These HST COS/G130M spectra show a wide variety of Ly α profiles, including damped absorption, Ly α emission in DLA profiles, P Cygni profiles, and pure Ly α emission. We attribute the damped absorption to Ly α photons being scattered out of the spectroscopic aperture, and we argue that the especially large diversity among CLASSY Ly α profiles can be largely attributed to large

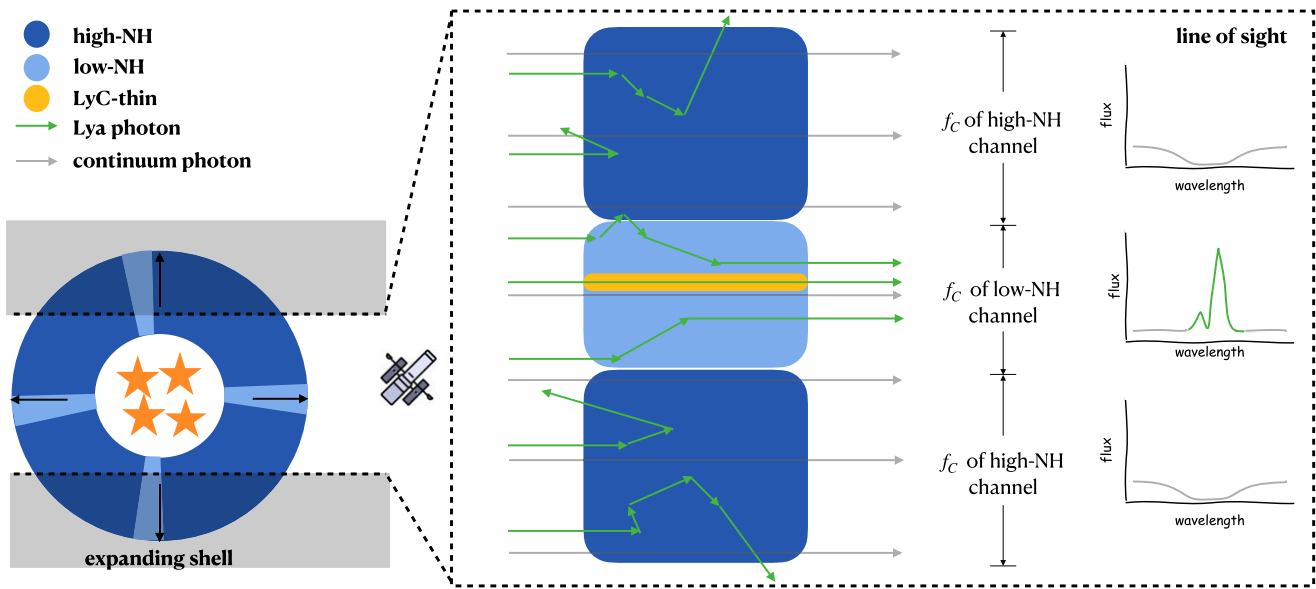


Figure 17. The left panel shows the side view of HST/COS observation. We adopt a continuous shell geometry, which contains different column-density regions as dark blue and light blue. This is somewhat an oversimplification as the ISM can be clumpy, but should be the simplest way to illustrate the ISM in galaxies. We note the scale length of different regions in this figure does not indicate their physical scale length. We use the gray shaded regions to indicate the parts that are missed by the HST/COS aperture. The right panel shows the zoom-in structure of a small slab of the outflowing shell. The yellow, light blue, and dark blue indicate the LyC-thin, low- $N_{\text{H I}}$, and high- $N_{\text{H I}}$ paths, respectively. The gray and green lines show the radiative transfer processes of the continuum and Ly α photons. We mark the covering fraction of different column density channels. The rightmost spectra represent the emergent Ly α profiles along different regions. The low- $N_{\text{H I}}$ channels lead to the Ly α emission line, but the high- $N_{\text{H I}}$ channels lead to the DLA system. The observed Ly α spectrum is a combination of those Ly α profiles, and thus, the residual flux in the bottom of the DLA profile equals the covering fraction of low- $N_{\text{H I}}$ channels.

range of physical scales subtended by the COS aperture, a little over 100 pc up to nearly 8 kpc.

We separated the DLA and Ly α emission components of the profiles. Specifically, we adopted the precisely measured Doppler shifts of the O I absorption components as priors for the Doppler shift of each broad DLA profile, and we fitted the damped Ly α absorption with modified Voigt profiles. After subtracting the stellar continuum and the DLA profile, we modeled the Ly α emission profile and the appropriate underlying continuum using the shell model. For the first time, we measure the properties in the neutral shell traversed by the emergent Ly α emission, and the conditions in the high-column density clouds, in the same sample of galaxies. For double-peaked Ly α emission-line profiles, we defined the Doppler shift of the minimum between the two emission lines as the *trough velocity*, which we compared to the Doppler shifts of LIS absorption lines and the DLA. Our results are summarized below:

1. The Ly α emission in the bottom of the DLA profile reveals the inhomogeneity of the ISM and the outflows. The DLA profile and Ly α emission line can be surprisingly well fitted by simply splitting a geometric covering factor between the high-column density sightlines and the lower- $N_{\text{H I}}$ channels through which Ly α photons escape. This suggests little Ly α exchange between high- and low- $N_{\text{H I}}$ paths. Combining the sightlines probed by Ly α emission lines with those producing damped absorption, the net distribution of column densities is bimodal and therefore qualitatively similar to the distributions predicted by numerical simulations of H I regions (Ma et al. 2020; Kakiichi & Gronke 2021). It is important to note, however, that this observed distribution is offset to higher $N_{\text{H I}}$ compared with the simulations. This discrepancy could arise from

gas on larger spatial scales than the simulations include, or from structural differences in the star-forming complexes; but, whatever its origin, an understanding of the offset will better inform our understanding of the channels through which not only Ly α but also LyC photons escape from galaxies.

2. We find that the Doppler shift of the Ly α trough velocity matches that of the Si II velocity in most galaxies with DLAs, suggesting that the Si II absorbers in those galaxies are mainly in neutral phase. However, for galaxies without DLA systems, the Ly α trough velocity is always smaller than the Si II velocity, suggesting Si II tracing a more ionized phase of the outflow, consistent with Xu et al. (2022). Thus, the Si II absorbers are multiphase, including neutral hydrogen in addition to the mostly ionized phase. Combining the Ly α and Si II, we are able to identify the ionization of Si II absorbers. Our comparison also suggests that the Ly α trough velocity directly measures the average velocity of neutral gas in the static ISM and outflows.
3. In spectra with a DLA, the Ly α trough velocity agrees well with the DLA velocity (O I velocity), suggesting that the high- $N_{\text{H I}}$ clouds have similar kinematics as low- $N_{\text{H I}}$ clouds. Further, the Si II also agrees well with the DLA velocity, even for galaxies without Ly α emission. Thus, we conclude that Si II mainly traces the neutral gas in high- $N_{\text{H I}}$ columns if the galaxies show DLAs.
4. Motivated by the numerical simulations of Kakiichi & Gronke (2021), we combine the measurements of Ly α peak separation and Ly α red peak asymmetry in a diagnostic diagram that differentiates the type of channels for LyC leakage. Comparing the diagram with the known LyC leakers, we suggest that the boundary for distinguishing substantial leakage from small leakage is a peak

separation less than $\sim 400 \text{ km s}^{-1}$. In the case of leakage, or equivalently small peak separation, then the red peak asymmetry parameter distinguishes holes, where $A_f > 3$, from the more symmetric profiles generated by full breaks. Six CLASSY galaxies are identified as the density-bounded LyC leakers by this technique, agreeing with the selection of net Ly α trough flux. The inferred properties of the LyC-thin sightlines depend on galaxy orientation, whereas the [O III]/[O II] ratio offers a sightline-independent perspective. We confirm the presence of an inverse relation between Ly α peak separation and the [O III]/[O II] ratio, as has been noted previously (Jaskot et al. 2019; Flury et al. 2022).

5. Similar to Orlicová et al. (2018), we find that the fitted redshift is always larger than the spectroscopic redshift, and the fitted outflow velocity is larger by $10\text{--}200 \text{ km s}^{-1}$ than the Ly α trough velocity. The connection between the Ly α trough velocity and the outflow velocity offers new insight into the origin of those discrepancies, which we suggest are not adequately explained by parameter degeneracies (Li & Gronke 2022). We argue instead that aperture vignetting is the primary source of the discrepancies. The COS aperture vignettes the blueshifted peak more than the redshifted peak, resulting in a lower blue-to-red peak ratio. To match the lower blue-to-red peak ratio, the radiative transfer model requires a higher outflow velocity and, thus, a larger redshift to match the outflow velocity to Ly α trough velocity.

Our results underline the sensitivity of Ly α profiles to aperture vignetting. The COS aperture not only excludes a large fraction of Ly α photons; it modifies the Ly α profile. Like many CLASSY targets, the composite Ly α spectra of star-forming galaxies at $z \sim 1.8\text{--}3.5$ show DLA systems as well (Reddy et al. 2016, 2022). An important difference, however, is that the typical slit width used in ground-based spectroscopy, $1''.2$, corresponds to $\sim 10 \text{ kpc}$. The COS aperture subtends a comparable physical scale only for the most distant Lyman break analogs in CLASSY, and their COS spectra do not show DLAs. Nonetheless, our analysis suggests the DLAs appear in the $z \sim 2$ spectra because the Ly α escape on spatial scales is larger than the slit width. An important implication of this

paper is that aperture vignetting could strongly affect recent JWST observation of EoR galaxies using the near infrared spectrograph (NIRSPec) slit mode (Heintz et al. 2023), of which the slit width is just $0''.2$, corresponding to only $\sim 1 \text{ kpc}$.

In this paper, we leveraged these aperture effects, recognizing an opportunity to characterize the properties of the low- N_{HI} channels and high- N_{HI} clouds in the same set of galaxy sightlines. To fully understand the connection between the observed Ly α profile and LyC leakage, the radiative transfer simulations will need to predict the spatial variations in the profile shape. The extracted Ly α profiles used in this work, including the DLA profiles and the best-fit shell model spectra, can be downloaded from the CLASSY High Level Science Products database, which is developed and maintained at STScI, Baltimore, USA.²⁷

Acknowledgments

We thank the anonymous referee for the valuable comments. The CLASSY team is grateful for the support that was provided by NASA through grant HST-GO-15840, from the Space Telescope Science Institute, which is operated by the Associations of Universities for Research in Astronomy, Incorporated, under NASA contract NAS5-26555. C.L.M. thanks the NSF for support through AST-1817125. B.L.J. thanks support from the European Space Agency (ESA). The CLASSY collaboration extends special gratitude to the Lorentz Center for useful discussions during the ‘‘Characterizing Galaxies with Spectroscopy with a view for JWST’’ 2017 workshop that led to the formation of the CLASSY collaboration and survey.

Facility: HST (COS).

Software: astropy (The Astropy Collaboration 2013, 2018), CalCOS (STScI), Python.

Appendix Best-fit Ly α Spectra

Figures 18 and 19 present the best-fit Ly α spectra obtained using approaches described in Sections 3.2.1 and 3.2.2, respectively.

²⁷ The data is available at the CLASSY HLSP page at DOI:10.17909/m3fq-jj25 and <https://archive.stsci.edu/hlsp/classy>.

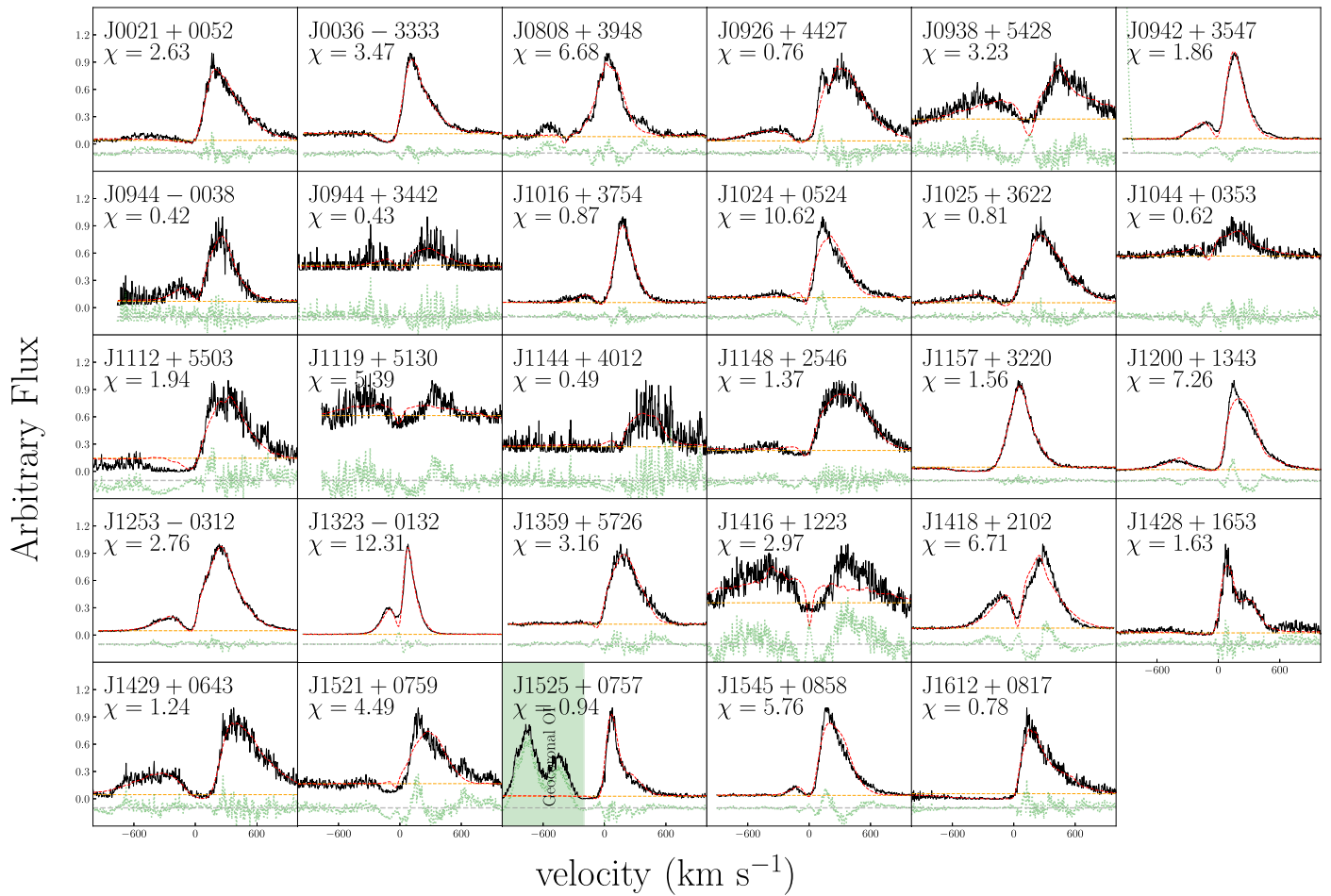


Figure 18. Best-fit Ly α spectra (red) for 29 CLASSY galaxies using the total stellar continuum and a Gaussian redshift prior with $\sigma = 120 \text{ km s}^{-1}$ (first attempt). The spectra are normalized by the peak flux, and the orange dashed lines indicate the continuum level for each object. Clearly, the Ly α spectra of J0938+5428, J0944+3442, J1044+0353, J1119+5130, J1144+4012, J1416+1223, and J1521+0759 have failed to be reproduced. We use the green lines to show the residual and manually shift it by -0.1 for better illustration. The gray dashed lines indicate the zero level of the residual.

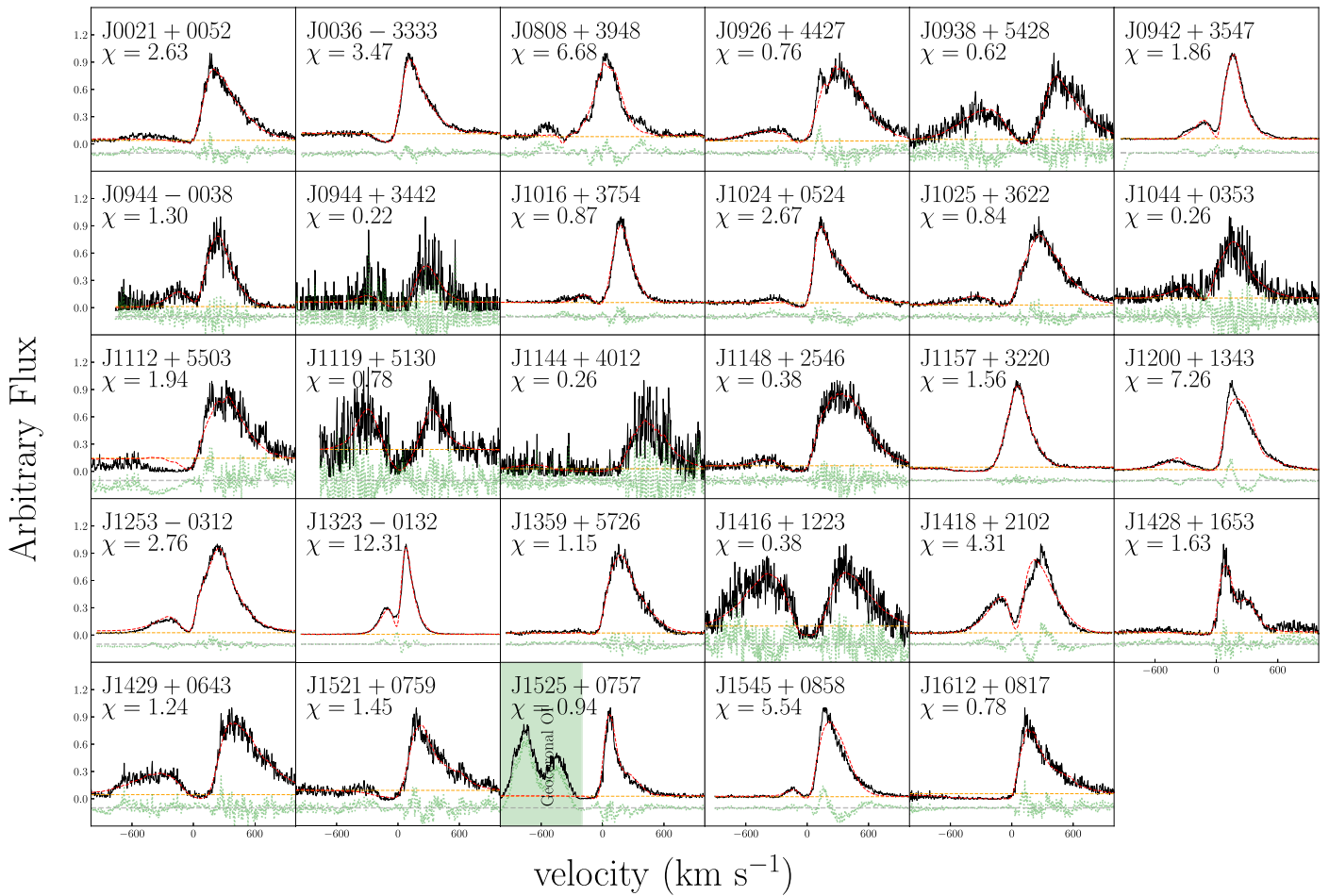


Figure 19. Best-fit Ly α spectra (red) for 29 CLASSY galaxies using the residual stellar continuum and a Gaussian redshift prior with $\sigma = 120 \text{ km s}^{-1}$ (second attempt). The spectra are normalized by the peak flux, and the orange dashed lines indicate the continuum level for each object. Every input Ly α profile is successfully reproduced by tlac model. We use the green lines to show the residual and manually shift it by -0.1 for better illustration. The gray dashed lines indicate the zero level of the residual.

ORCID iDs

Weida Hu <https://orcid.org/0000-0003-3424-3230>
 Crystal L. Martin <https://orcid.org/0000-0001-9189-7818>
 Max Gronke <https://orcid.org/0000-0003-2491-060X>
 Simon Gazagnes <https://orcid.org/0000-0002-5659-4974>
 Matthew Hayes <https://orcid.org/0000-0001-8587-218X>
 John Chisholm <https://orcid.org/0000-0002-0302-2577>
 Timothy Heckman <https://orcid.org/0000-0001-6670-6370>
 Matilde Mingozzi <https://orcid.org/0000-0003-2589-762X>
 Namrata Roy <https://orcid.org/0000-0002-4430-8846>
 Peter Senchyna <https://orcid.org/0000-0002-9132-6561>
 Xinfeng Xu <https://orcid.org/0000-0002-9217-7051>
 Danielle A. Berg <https://orcid.org/0000-0002-4153-053X>
 Bethan L. James <https://orcid.org/0000-0003-4372-2006>
 Daniel P. Stark <https://orcid.org/0000-0001-6106-5172>
 Karla Z. Arellano-Córdova <https://orcid.org/0000-0002-2644-3518>
 Alaina Henry <https://orcid.org/0000-0002-6586-4446>
 Anne E. Jaskot <https://orcid.org/0000-0002-6790-5125>
 Nimisha Kumari <https://orcid.org/0000-0002-5320-2568>
 Kaelee S. Parker <https://orcid.org/0000-0002-8809-4608>
 Claudia Scarlata <https://orcid.org/0000-0002-9136-8876>
 Aida Wofford <https://orcid.org/0000-0001-8289-3428>
 Ricardo O. Amorín <https://orcid.org/0000-0001-5758-1000>
 Jarle Brinchmann <https://orcid.org/0000-0003-4359-8797>

Cody Carr <https://orcid.org/0000-0003-4166-2855>
 Alessandra Aloisi <https://orcid.org/0000-0003-4137-882X>

References

- Alexandroff, R. M., Heckman, T. M., Borthakur, S., Overzier, R., & Leitherer, C. 2015, *ApJ*, **810**, 104
 Astropy Collaboration, Price-Whelan, A. M., Sipőcz, B. M., et al. 2018, *AJ*, **156**, 123
 Astropy Collaboration, Robitaille, T. P., Tollerud, E. J., et al. 2013, *A&A*, **558**, A33
 Berg, D. A., James, B. L., King, T., et al. 2022, *ApJS*, **261**, 31
 Brocklehurst, M. 1971, *MNRAS*, **153**, 471
 Bruzual, G., & Charlot, S. 2003, *MNRAS*, **344**, 1000
 Bunker, A. J., Saxena, A., Cameron, A. J., et al. 2023, *A&A*, **677**, A88
 Cardelli, J. A., Clayton, G. C., & Mathis, J. S. 1989, *ApJ*, **345**, 245
 Cash, W. 1979, *ApJ*, **228**, 939
 Chevalier, R. A., & Clegg, A. W. 1985, *Natur*, **317**, 44
 Chisholm, J., Gazagnes, S., Schaerer, D., et al. 2018, *A&A*, **616**, A30
 Chisholm, J., Rigby, J. R., Bayliss, M., et al. 2019, *ApJ*, **882**, 182
 Chisholm, J., Tremonti, C. A., Leitherer, C., et al. 2015, *ApJ*, **811**, 149
 Dijkstra, M. 2014, *PASA*, **31**, e040
 Dijkstra, M., Gronke, M., & Venkatesan, A. 2016, *ApJ*, **828**, 71
 Dijkstra, M., Haiman, Z., & Spaans, M. 2006, *ApJ*, **649**, 14
 Draine, B. T. 2011, *Physics of the Interstellar and Intergalactic Medium* (Princeton, NJ: Princeton Univ. Press)
 Eide, M. B., Gronke, M., Dijkstra, M., & Hayes, M. 2018, *ApJ*, **856**, 156
 Erb, D. K., Li, Z., Steidel, C. C., et al. 2023, *ApJ*, **953**, 118
 Erb, D. K., Steidel, C. C., & Chen, Y. 2018, *ApJL*, **862**, L10
 Fielding, D. B., & Bryan, G. L. 2022, *ApJ*, **924**, 82

- Finkelstein, S. L., D'Aloisio, A., Paardekooper, J.-P., et al. 2019, *ApJ*, **879**, 36
- Flury, S. R., Jaskot, A. E., Ferguson, H. C., et al. 2022, *ApJ*, **930**, 126
- Gazagnes, S., Chisholm, J., Schaerer, D., Verhamme, A., & Izotov, Y. 2020, *A&A*, **639**, A85
- Gordon, K. D., Clayton, G. C., Misselt, K. A., Landolt, A. U., & Wolff, M. J. 2003, *ApJ*, **594**, 279
- Gronke, M., Bull, P., & Dijkstra, M. 2015, *ApJ*, **812**, 123
- Gronke, M., & Dijkstra, M. 2014, *MNRAS*, **444**, 1095
- Gronke, M., Dijkstra, M., McCourt, M., & Oh, S. P. 2016, *ApJL*, **833**, L26
- Gronke, M., Dijkstra, M., McCourt, M., & Oh, S. P. 2017, *A&A*, **607**, A71
- Gronke, M., & Oh, S. P. 2020, *MNRAS*, **492**, 1970
- Gurung-López, S., Gronke, M., Saito, S., Bonoli, S., & Orsi, Á. A. 2022, *MNRAS*, **510**, 4525
- Hansen, M., & Oh, S. P. 2006, *MNRAS*, **367**, 979
- Hartmann, D., & Burton, W. B. 1997, *Atlas of Galactic Neutral Hydrogen* (Cambridge: Cambridge Univ. Press)
- Hayes, M., Östlin, G., Duval, F., et al. 2014, *ApJ*, **782**, 6
- Hayes, M., Östlin, G., Schaerer, D., et al. 2013, *ApJL*, **765**, L27
- Hayes, M. J., Runnholm, A., Scarlata, C., Gronke, M., & Rivera-Thorsen, T. E. 2023, *MNRAS*, **520**, 5903
- Hayes, M. J., & Scarlata, C. 2023, *ApJL*, **954**, L14
- Heckman, T. M., Borthakur, S., Overzier, R., et al. 2011, *ApJ*, **730**, 5
- Heckman, T. M., Lehnert, M. D., Strickland, D. K., & Armus, L. 2000, *ApJS*, **129**, 493
- Heintz, K., Watson, D., & Brammer, G. 2023, arXiv:2306.00647
- Henry, A., Scarlata, C., Martin, C. L., & Erb, D. 2015, *ApJ*, **809**, 19
- Hu, W., Wang, J., Infante, L., et al. 2021, *NatAs*, **5**, 485
- Izotov, Y. I., Schaerer, D., Thuan, T. X., et al. 2016, *MNRAS*, **461**, 3683
- Izotov, Y. I., Schaerer, D., Worseck, G., et al. 2018a, *MNRAS*, **474**, 4514
- Izotov, Y. I., Schaerer, D., Worseck, G., et al. 2020, *MNRAS*, **491**, 468
- Izotov, Y. I., Worseck, G., Schaerer, D., et al. 2018b, *MNRAS*, **478**, 4851
- James, B. L., Berg, D. A., King, T., et al. 2022, *ApJS*, **262**, 37
- Jaskot, A. E., Dowd, T., Oey, M. S., Scarlata, C., & McKinney, J. 2019, *ApJ*, **885**, 96
- Jaskot, A. E., & Oey, M. S. 2013, *ApJ*, **766**, 91
- Kakiichi, K., & Gronke, M. 2021, *ApJ*, **908**, 30
- Kewley, L. J., Nicholls, D. C., & Sutherland, R. S. 2019, *ARA&A*, **57**, 511
- Klein, R. I., McKee, C. F., & Colella, P. 1994, *ApJ*, **420**, 213
- Kourkchi, E., Courtois, H. M., Graziani, R., et al. 2020, *AJ*, **159**, 67
- Kulas, K. R., Shapley, A. E., Kollmeier, J. A., et al. 2012, *ApJ*, **745**, 33
- Labbe, I., van Dokkum, P., Nelson, E., et al. 2023, *Natur*, **616**, 266
- Leitherer, C., Schaerer, D., Goldader, J. D., et al. 1999, *ApJS*, **123**, 3
- Li, Z., & Gronke, M. 2022, *MNRAS*, **513**, 5034
- Li, Z., Steidel, C. C., Gronke, M., Chen, Y., & Matsuda, Y. 2022, *MNRAS*, **513**, 3414
- Lin, X., Cai, Z., Zou, S., et al. 2023, *ApJL*, **944**, L59
- Looser, T. J., D'Eugenio, F., Maiolino, R., et al. 2023, arXiv:2302.14155
- Ma, X., Quataert, E., Wetzel, A., et al. 2020, *MNRAS*, **498**, 2001
- Martin, C. L., Dijkstra, M., Henry, A., et al. 2015, *ApJ*, **803**, 6
- Martin, C. L., Shapley, A. E., Coil, A. L., et al. 2012, *ApJ*, **760**, 127
- Martini, P., Leroy, A. K., Mangum, J. G., et al. 2018, *ApJ*, **856**, 61
- Mason, C. A., Fontana, A., Treu, T., et al. 2019, *MNRAS*, **485**, 3947
- McKinney, J. H., Jaskot, A. E., Oey, M. S., et al. 2019, *ApJ*, **874**, 52
- Michel-Dansac, L., Blaizot, J., Garel, T., et al. 2020, *A&A*, **635**, A154
- Mingozzi, M., James, B. L., Arellano-Córdova, K. Z., et al. 2022, *ApJ*, **939**, 39
- Naidu, R. P., Tacchella, S., Mason, C. A., et al. 2020, *ApJ*, **892**, 109
- Nakajima, K., & Ouchi, M. 2014, *MNRAS*, **442**, 900
- Neufeld, D. A. 1990, *ApJ*, **350**, 216
- Orlitová, I., Verhamme, A., Henry, A., et al. 2018, *A&A*, **616**, A60
- Ouchi, M., Ono, Y., & Shibuya, T. 2020, *ARA&A*, **58**, 617
- Partridge, R. B., & Peebles, P. J. E. 1967, *ApJ*, **147**, 868
- Plat, A., Charlot, S., Bruzual, G., et al. 2019, *MNRAS*, **490**, 978
- Prochaska, J. X. 2019, in *HI Absorption in the Intergalactic Medium*, ed. A. Verhamme et al. (Berlin: Springer), 111
- Prochaska, J. X., O'Meara, J. M., Fumagalli, M., Bernstein, R. A., & Burles, S. M. 2015, *ApJS*, **221**, 2
- Reddy, N. A., Steidel, C. C., Pettini, M., & Bogosavljević, M. 2016, *ApJ*, **828**, 107
- Reddy, N. A., Topping, M. W., Shapley, A. E., et al. 2022, *ApJ*, **926**, 31
- Rhoads, J. E., Dey, A., Malhotra, S., et al. 2003, *AJ*, **125**, 1006
- Rivera-Thorsen, T. E., Hayes, M., Östlin, G., et al. 2015, *ApJ*, **805**, 14
- Robertson, B. E., Ellis, R. S., Furlanetto, S. R., & Dunlop, J. S. 2015, *ApJL*, **802**, L19
- Runnholm, A., Gronke, M., & Hayes, M. 2021, *PASP*, **133**, 034507
- Saldana-Lopez, A., Schaerer, D., Chisholm, J., et al. 2022, *A&A*, **663**, A59
- Saxena, A., Robertson, B. E., Bunker, A. J., et al. 2023, arXiv:2302.12805
- Schneider, E. E., & Robertson, B. E. 2018, *ApJ*, **860**, 135
- Senchyna, P., Plat, A., Stark, D. P., & Rudie, G. C. 2023, arXiv:2303.04179
- Steidel, C. C., Bogosavljević, M., Shapley, A. E., et al. 2011, *ApJ*, **736**, 160
- Tang, M., Stark, D. P., Chen, Z., et al. 2023, *MNRAS*, in press
- Tilvi, V., Malhotra, S., Rhoads, J. E., et al. 2020, *ApJL*, **891**, L10
- Trainor, R. F., Strom, A. L., Steidel, C. C., et al. 2019, *ApJ*, **887**, 85
- Verhamme, A., Dubois, Y., Blaizot, J., et al. 2012, *A&A*, **546**, A111
- Verhamme, A., Orlitová, I., Schaerer, D., & Hayes, M. 2015, *A&A*, **578**, A7
- Verhamme, A., Schaerer, D., & Maselli, A. 2006, *A&A*, **460**, 397
- Xie, Y., Hao, L., & Li, A. 2014, *ApJL*, **794**, L19
- Xu, X., Heckman, T., Henry, A., et al. 2022, *ApJ*, **933**, 222
- Xu, X., Heckman, T., Henry, A., et al. 2023, *ApJ*, **948**, 28
- Yang, H., Malhotra, S., Gronke, M., et al. 2016, *ApJ*, **820**, 130
- Yang, H., Malhotra, S., Gronke, M., et al. 2017, *ApJ*, **844**, 171
- Yuan, Y., Krumholz, M. R., & Martin, C. L. 2023, *MNRAS*, **518**, 4084
- Zheng, Z., Cen, R., Trac, H., & Miralda-Escudé, J. 2010, *ApJ*, **716**, 574
- Zheng, Z., Cen, R., Weinberg, D., Trac, H., & Miralda-Escudé, J. 2011, *ApJ*, **739**, 62